Rhodes University

Foreground simulations for observations of the global 21-cm signal

Author: Diana Klutse

Supervisors: Prof. Gianni Bernardi,
Prof. Oleg M. Smirnov,
Dr. Chuneeta D. Nunhokee

A thesis submitted in fulfilment of the requirements for the degree of Master of Science

in the

RHODES UNIVERSITY
Where leaders learn

Centre for Radio Astronomy Techniques and Technologies
Department of Physics and Electronics

August, 2018

Abstract

The sky-averaged (global) spectrum of the redshifted 21-cm line promises to be a direct probe of the Dark Ages, the period before the first luminous sources formed and the Epoch of Reionization during which these sources produced enough ionizing photons to ionize the neutral intergalactic medium. However, observations of this signal are contaminated by both astrophysical foregrounds which are orders of magnitude brighter than the cosmological signal and by non-astrophysical and non-ideal instrumental effects. It is therefore crucial to understand all these data components and their impacts on the cosmological signal, for successful signal extraction. In this view, we investigated the impact that small scale spatial structures of diffuse Galactic foreground has on the foreground spectrum as observed by a global 21-cm observation.

We simulated two different sets of observations using a realistic dipole beam model of two synchotron foreground templates that differ from each other in the small scale structure: the original 408 MHz all-sky map by Haslam et al. (1982) and a version where the calibration was improved to remove artifcats and point sources (Remazeilles et al., 2015). We generated simulated foreground spectra and modeled them using a polynomial expansion in frequency. We found that the different foreground templates have a modest impact on the simulated spectra, generate differences up to 2% in the root mean square of residual spectra after the log-polynomial best fit was subtracted out.

Acknowledgements

I wish to bring to recognition all those who supported me in one way or the other during this Academic Journey. The list is certainly a tall one! I therefore in advance wish to express my sincerest apologies to anyone who might feel left out.

I would like to first of all commend my academic advisor Prof. Gianni Bernardi, who has been a pillar and a teacher throughout this entire journery and his entire family. My special acknowledgement also goes Prof. Oleg M. Smirnov and to Dr. Chuneeta D. Nunhokee for her guidance and direction towards the realization of this work.

My heartfelt gratitude also goes to the entire of Physics and Electronics Department of the Rhodes University especially the Head of Department Prof. Chinthambo for all his advise and support during my study. To Ronel, Sindi and Michelle, I say a big thank you for carrying out all the administrative work that was related to this work. Thank you Cyril and Andrew for getting my workstation always ready and in good condition. Without you guys in the faculty, life couldn't have been easier.

To all my colleague researchers, Mr. Theophilus Narh, Mr. Akoto-Danso Alexander, Mr. Iheanatu Kelachukwu Joseph, Robert, Kwazi, Gift, Ulrich, Mark, Siyanda, Eric, James, Liju, Philip, Lerato, Cyinde, Lexi, Samuel, Lerato and Esther I say you guys are wonderful team players and you are in fact more than just colleagues. You made my stay on campus felt like home. Thank you so much for all the academic support in every form and shape.

Thanks to Mrs. Chidima Iheanatu and Mrs. Akoto-Danso Audrey for the moral support during all the difficult moments. It was an awesome experience having you by my side in such times. You are simply amazing! My appreciation also goes to the entire membership of the Rock Family Church in Grahamstown for their love and prayers especially my two mums; Deana and Brenda as well as Tata Shaun.

I am also extremely grateful to my parents Mr. and Mrs. Tettegah for all the training and upbringing. To my siblings Precious, Linda, Stella and Daniel, I say God bless you for always being ready and willing to throw your weights behind me.

Words cannot express how grateful I am to my husband Mr. Evans Asare Yeboah for standing by me throughout all these years. Finally to my daughter Aliza Afia Asabea Yeboah, I say thank you for those sleepless nights you gave me. It made me really go an extra mile for getting this work done.

To my parents...

Declaration of Authorship

I, Diana Klutse, declare that this thesis titled, '*Foreground simulations for observations of the global 21-cm signal*' and the work presented in it are my own. I confirm that:

- This work was done wholly or mainly while in candidature for a research degree at this University.
- Where any part of this thesis has previously been submitted for a degree or any other qualification at this University or any other institution, this has been clearly stated.
- Where I have consulted the published work of others, this is always clearly attributed.
- Where I have quoted from the work of others, the source is always given. With the exception of such quotations, this thesis is entirely my own work.
- I have acknowledged all main sources of help.
- Where the thesis is based on work done by myself jointly with others, I have made clear exactly what was done by others and what I have contributed myself.

Signed:

_____

Date:

_____

Contents

Physical Constants

Speed of light	c	$=$	2.99792458×10^{8} ms^{-1}
Boltzmann constant	k	$=$	$1.3806488 \times 10^{-23}$ m^{2} kg s^{2} K^{-1}
Plancks's constant	h	$=$	$6.62606957 \times 10^{-34}$ m^{-2} kg s^{-1}

Chapter 1

Introduction

The transition of the Universe from the dark ages, when the universe was completely neutral following hydrogen recombination through the epoch of reionization (EoR), when the first stars and galaxies started emitting ultra-violet and X-ray radiation, thereby reionizing the surrounding neutral medium (see Figure 1.1), remains one of the least constrained frontiers of modern cosmology (e.g., Pritchard & Loeb, 2010). Observations of the redshifted 21-cm signal generated by the spin flip transition of neutral hydrogen (HI) promise to be a direct probe of the EoR (Iliev et al., 2002; Madau et al., 1997; Scott & Rees, 1990; Tozzi et al., 2000).

Most of the current observational efforts seek to measure the fluctuations in the 21-cm signal via power spectrum measurements, e.g. the Murchison Widefield Array (MWA, Tingay et al., 2013), the Precision Array for Probing the Epoch of Reionization (PAPER, Parsons et al., 2010), the Low Frequency Array (LOFAR, Rottgering et al., 2006) and the Giant Metrewave Radio Telescope Epoch of Reionization (GMRT-EoR, Paciga et al., 2011). Due the intrinsic faintness of the EoR signal, such experiments require many hundreds of hours of observation in order to attempt a detection.

Alternatively, observations of the global (where the signal is averaged over all directions in the sky) 21-cm signal can achieve the required sensitivity in a few tens of hours only. Ongoing global signal experiments include the Experiment to Detect the Global EoR Signature (EDGES, Bowman & Rogers, 2010; Monsalve et al., 2017), the Large aperture Experiment to detect the Dark Ages (LEDA, Bernardi et al., 2016; Greenhill & Bernardi, 2012; Price et al., 2018), the Broadband Instrument for Global HydrOgen ReioNisation Signal, (BIGHORNS, Sokolowski et al., 2015), the Sonda Cosmológica de las Islas para la Detección de Hidrógeno Neutro (SCI-HI, Voytek et al., 2014) and the Shaped Antenna Measurement of background RAdio Spectrum (SARAS, Singh et al., 2017). In the future, the Dark Ages Radio Explorer (DARE, Burns et al., 2017) is a

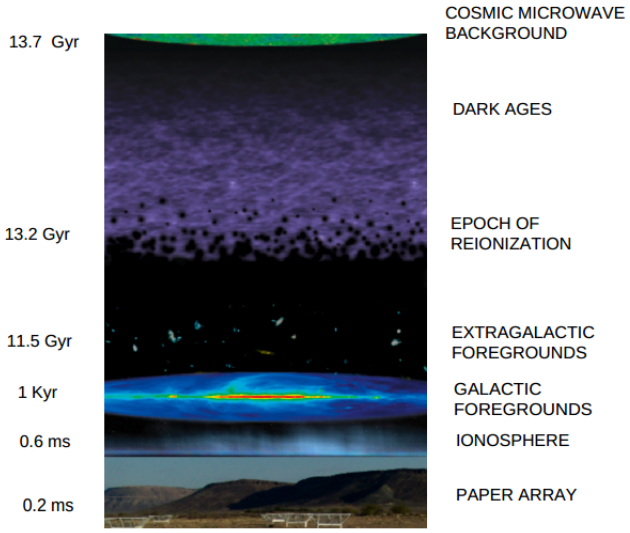

FIGURE 1.1: A cartoon representation of the various sources of radiation observed in a 21-cm experiment: the cosmic microwave background radiation, the 21-cm emission originating from either the dark ages or the epoch of reionization and extragalactic and Galactic foreground emission that is generated more locally. Before the signal is recorded from an interferometric array, it may suffer from distortions when passing through our own ionosphere, inview of this current work is underway to mitigate it (adapted from Jelić, 2010).

proposed space mission to measure the sky-averaged signal from the dark ages to the end of the EoR in the $6 < z < 30$ range. The next section offers an overview of the global 21-cm signal.

1.1 Global signal Overview

The 21-cm line emerges from the electron spin flip relative to the nucleus, where the electron-proton parallel-parallel state has slightly higher energy than its parallel-antiparallel state. The transition between these two states leads to the emission of a photon with rest frame frequency $\nu \sim 1420$ MHz, equivalent to a wavelength of 21 cm (Figure 1.2 displays an artistic view of this transition). However if this 21-cm signal is radiated by a cloud at high redshift, the wavelength will be stretched by a factor of $(1 + z)$ (Fialkov & Loeb, 2013; Furlanetto et al., 2006; Pritchard & Loeb, 2012) and will be observed in the meter wavelength regime.

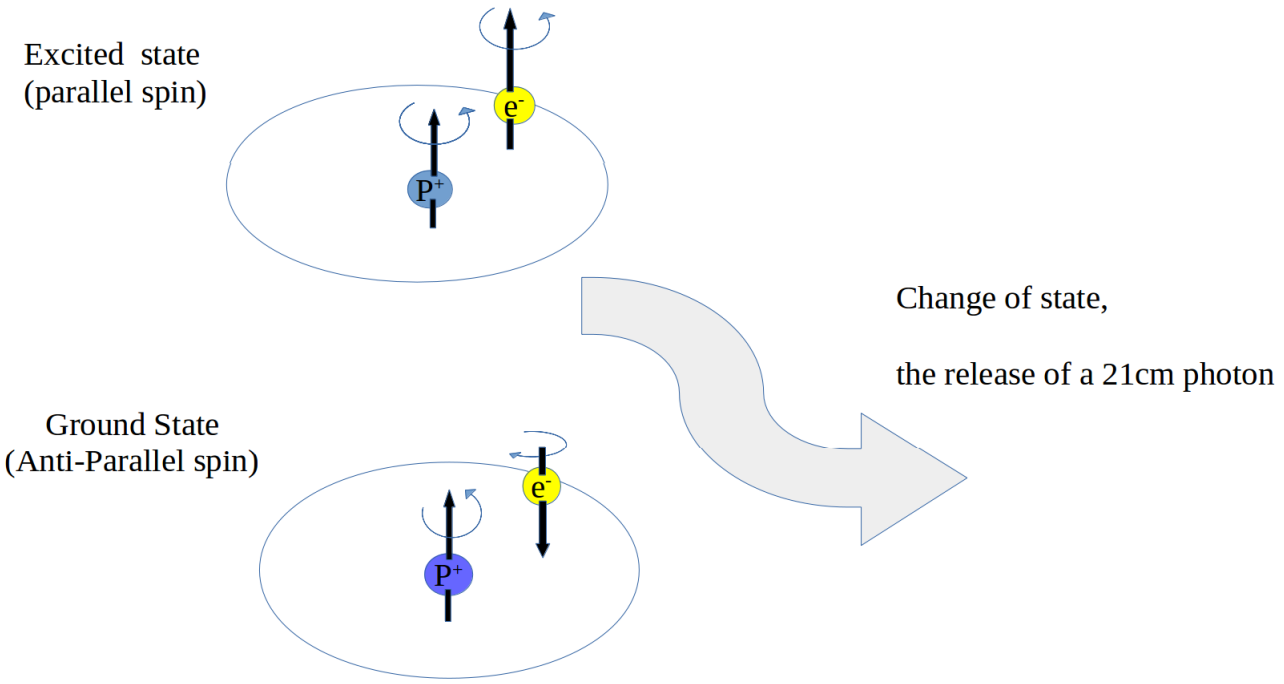

FIGURE 1.2: An artistic view of the spin flip transition of the neutral hydrogen, where the electron-proton parallel-parallel state has slightly higher energy than its parallel-antiparallel state. The difference in these energy levels results in the emission of the 21-cm signal.

The 21-cm brightness temperature T_b at redshift z can be expressed as (Furlanetto, 2006):

$$\delta T_b \approx 27\, x_{HI}\, (1+\delta_b)\, \frac{\Omega_b h^2}{0.023} \left(\frac{0.15}{\Omega_m h^2} \frac{1+z}{10} \right)^{\frac{1}{2}} \left(\frac{T_s - T_\gamma}{T_s} \right) \text{ mK}, \tag{1.1}$$

where x_{HI} is the Hydrogen neutral fraction, δ_b denotes the baryon density contrast, Ω_m and Ω_b the matter and baryon density respectively, h the Hubble parameter, T_s the spin temperature that defines the relative populations of the two spin states and T_γ the Cosmic Microwave Background (CMB) temperature. Equation 1.1 shows that the 21-cm signal can be detected only as a contrast against the CMB background, i.e. if $T_s \neq T_\gamma$. In particular, if $T_s > T_\gamma$ ($T_s < T_\gamma$) the 21-cm can be seen in emission (absorption) against the CMB where the spin temperature is the weighted sum of three different components (Furlanetto et al., 2006):

$$T_s^{-1} = \frac{T_\gamma^{-1} + x_c T_K^{-1} + x_\alpha T_c^{-1}}{1 + x_c + x_\alpha}, \tag{1.2}$$

x_c and x_α are coupling coefficients for collisions and UV scattering respectively, T_K is the gas kinetic temperature and T_c the colour temperature of the Lyα radiation (Fialkov & Loeb, 2013; Furlanetto et al., 2006). There are basically three processes that establish the spin temperature (Furlanetto, 2016; Furlanetto et al., 2006):

- absorption (and stimulated emission) of CMB photons. Such interactions speedily bring the spin temperature to thermal equilibrium, i.e. $T_s = T_\gamma$, making the 21-cm signal unobservable;

- atomic collisions. Collisions may cause spin-flip transitions and, in the high redshift Universe, this mechanism efficiently couples the spin temperature to the gas temperature;

- resonant scattering of Lyα photons, also known as Wouthuysen-Field (WF) effect (Field, 1959; Wouthuysen, 1952, Figure 1.3). Qualitatively, the WF effect can be described as the absorption of a Lyα photon that excites an HI atom to the $2P$ state. De-excitation can happen in two stages: first through the emission of a shorter wavelength photon that leads the electron to the hyperfine HI level and, consequently, through the emission of a 21-cm photon. When the first stars begin to shine in our Universe, the WF effect quickly couple the spin temperature to the gas temperature, generating 21-cm radiation.

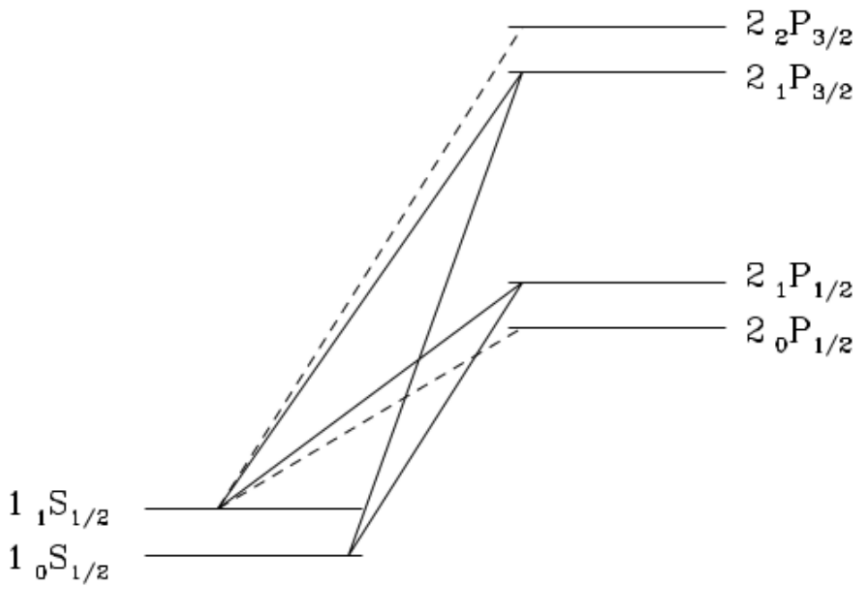

FIGURE 1.3: The hyperfine splittings of both the 1S and 2P levels of the neutral hydrogen atom relevant for the Wouthuysen-Field effect. The solid lines indicates allowed spin flip transitions while the dashed lines shows allowed transitions that do not result in spin flips. (from Furlanetto, 2016; Pritchard & Loeb, 2012).

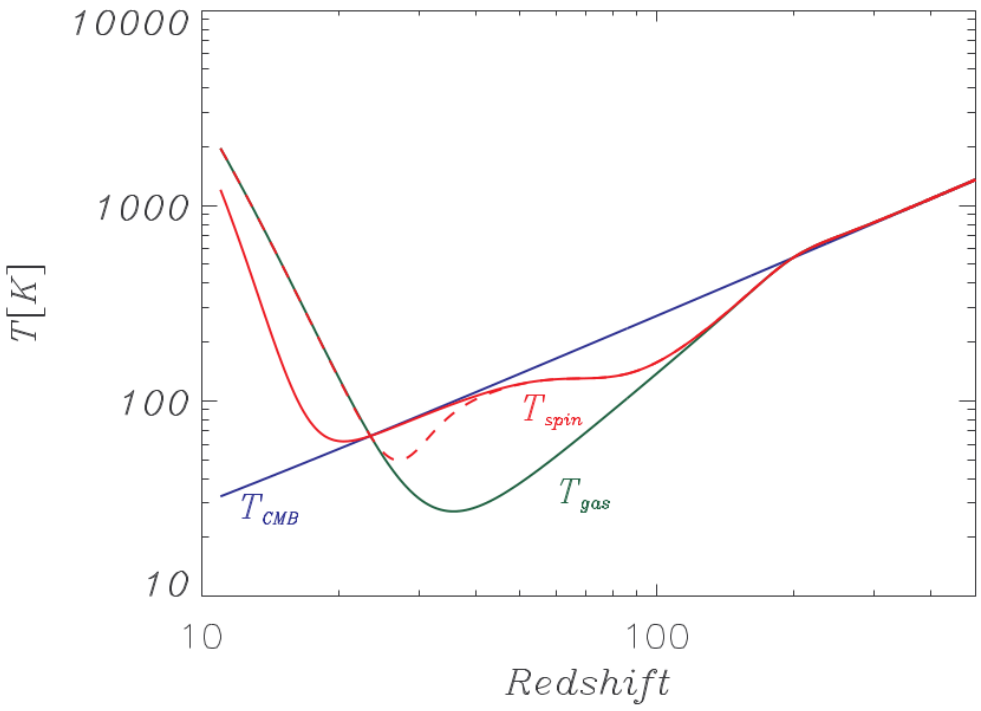

FIGURE 1.4: Model for the evolution of the CMB (blue line), gas (green line) and spin temperature (red solid line and red dashed line). Considering two senarious when the first astrophysical sources switch on and are expected to heat and ionize the InterGalactic Medium (IGM). Red dashed line: the spin temperature couples to the gas as the IGM is heated. Red solid line: the spin temperature couples to the gas after the IGM is heated (from Zaroubi, 2012). The most important features are the coupling between the spin temperature to the gas temperature (expected around $z \sim 25$ in this model) and the gas heating well above the CMB (occuring at $z > 10$ in this model).

1.1.1 The evolution of the global 21-cm signal

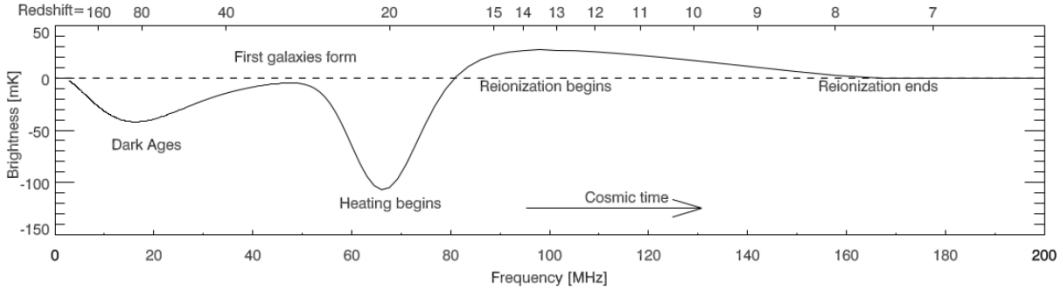

FIGURE 1.5: The evolution of the sky-averaged 21-cm brightness temperature (from Pritchard & Loeb, 2012).

The evolution of the global 21-cm signal depends, therefore, upon the combined evolution of the spin, gas and CMB temperatures, a tale of three temperatures (visualized in Figure 1.4). Figure 1.5 shows the redshift evolution of the global 21-cm signal for what

can be considered a reference model (Pritchard & Loeb, 2012). A few epoch are clear landmarks in the global signal evolution:

- Dark Ages ($30 \lesssim z \lesssim 200$): after recombination, the IGM cools adiabatically, i.e. quicker than the CMB, and it is sufficiently dense to couple the spin temperature to the gas temperature, i.e. $T_s = T_k < T_\gamma$ (e.g., Loeb & Zaldarriaga, 2004). The 21-cm brightness temperature shows, therefore, an absorption profile that peaks at $z \sim 80$. As the Universe expands, however, collisional coupling is no longer effective and the spin temperature is driven to the CMB temperature, leading the signal to eventually disappear ($z \sim 30$);

- First galaxies form ($z \sim 30$): first galaxies are expected to form in the first dark matter halos and their ultraviolet radiation quickly couples the spin temperature to the gas temperature through the WF effect (Field, 1959). As the gas is still colder than the CMB, the 21-cm signal becomes progressively brighter against the CMB with decreasing redshift. The details of such evolution depend on the details of the model physics. For instance, if most of the first stars are very massive, almost metal-free (POP III) rather than Solar mass-like (POP II), they will have a much higher ionizing efficiency and generate an earlier and deeper peak in the 21-cm signal (Furlanetto et al., 2006) compared to what is shown in Figure 1.5. Conversely, radiation or mechanical feedback can supress star formation in the fragile environment of these early galaxies, leading to a later peak in the 21-cm signal (Cohen et al., 2000; Fialkov et al., 2014);

- Heating begins ($z \sim 20$): first stellar black holes are expected to be created as the endpoint of stellar evolution. Stellar black holes in binary systems will start emitting X-rays through accretion: X-rays can travel further out in the IGM before they interact with an HI atom and can therefore heat the gas more uniformly (Pritchard & Furlanetto, 2007). The heating process depends upon the properties of the X-ray sources, e.g. it will take longer to heat the gas if X-ray binaries have low emissivity, leading to a deeper and wider absorption trough (Pritchard & Loeb, 2012). X-ray radiation will eventually heat the gas above the CMB ($T_s = T_k > T_\gamma$) and the 21-cm signal will be seen in emission ($z \sim 15$, Morandi & Barkana, 2012);

- Reionization begins ($z \sim 14$): continued star formation within galaxies generates enough ultraviolet background to escape the host galaxy and begins ionizing the surrounding IGM. Although the details of how reionization progresses are still the focus of intense theoretical studies, most studies show that denser regions are expected to ionize first, with ionized regions then merging together as reionization progresses (Ciardi et al., 2003);

- Reionization ends ($z \sim 7$): The HI fraction keeps declining as sources continue to ionize the IGM, until the neutral fraction approaches zero around $z \sim 7$ and the 21-cm signal disappears (this can be visualized in Figure 1.6.)

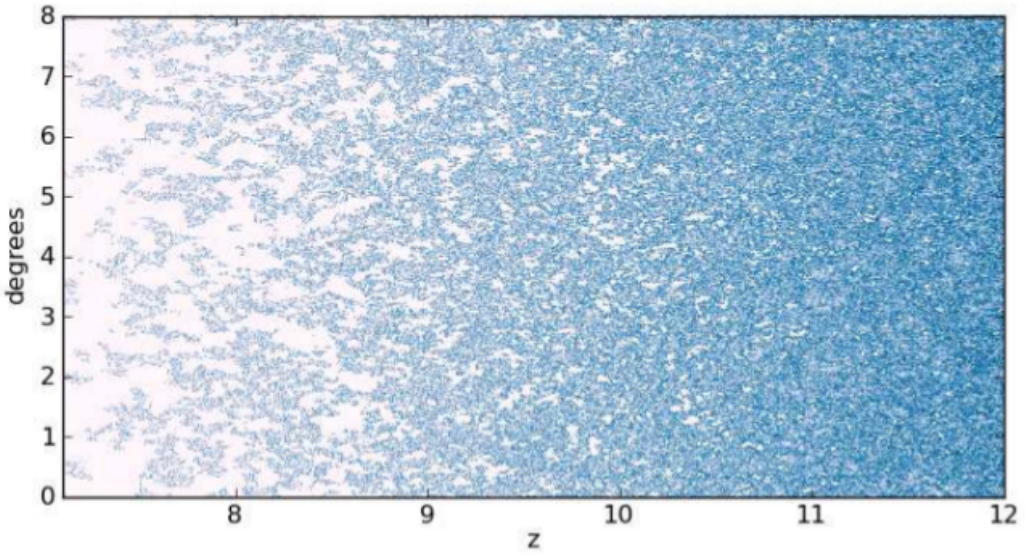

FIGURE 1.6: A 3 Mpc slice of a 1300 Mpc wide simulation of the 21-cm brightness temperature (from McQuinn & Switzer, 2009). The Hydrogen neutral fraction keeps declining as the ionizing sources continue in ionizing the IGM, until the neutral fraction approaches zero - ionized regions are shown in white. At $z \sim 7$ only small pockets of neutral Hydrogen are left.

Several authors have studied the impact of different model parameters on the global 21-cm signal. Here we summarize the study case from Mirocha et al. (2015) where four main parameters were identified: the minimum mass of dark matter halos for forming stars $T_{\rm min}$, the X-ray efficiency $\xi_{\rm X}$, the Lyman-Werner background efficiency $\xi_{\rm LW}$ and the ionizing efficiency $\xi_{\rm ion}$. Figure 1.7 shows that the $T_{\rm min}$ has the biggest impact on the position of the absorption trough in the 21-cm spectrum. Indeed, a smaller $T_{\rm min}$ value implies that star formation begins in less massive halos that form at earlier epochs than more massive ones, "shifting" the trough in 21-cm spectrum at higher redshift. We note that variations in $T_{\rm min}$ do not significantly change the 21-cm spectrums shape but just act as a clock, shifting the whole spectrum forward or backward.

The X-ray efficiency $\xi_{\rm X}$ regulates the amount of X-ray photons that are produced and injected in the IGM and, therefore, times the heating process: the higher $\xi_{\rm X}$ the quicker the IGM heating leading to a shallower trough and a transition to the 21-cm in emission against the CMB at earlier redshift. The X-ray efficiency therefore affects the position (although not us much as $T_{\rm min}$) and, more prominently, the shape of the 21-cm absorption profile.

The ionizing efficiency $\xi_{\rm ion}$ essentially sets the number of ionizing photons that escape from the galaxies into the IGM and is, therefore, the main parameter responsible for the reionization process. As it can indeed be seen in Figure 1.7, variations in the ionizing efficiency are only relevant once widespread ionization starts and the gas has been heated above the CMB and their impact is relatively straightforward to understand: higher ionizing efficiencies flood the IGM with more ionizing photons and, therefore, make reionization proceed more rapidly.

Finally the Lyman-Werner background efficiency $\xi_{\rm LW}$ accounts for the number of photons between 10.2 and 13.5 eV responsible for the WF coupling. If the Lyman-Werner background efficiency increases, the WF coupling between the spin and the gas temperature occurs more rapidly, moving the absorption trough at higher redshift.

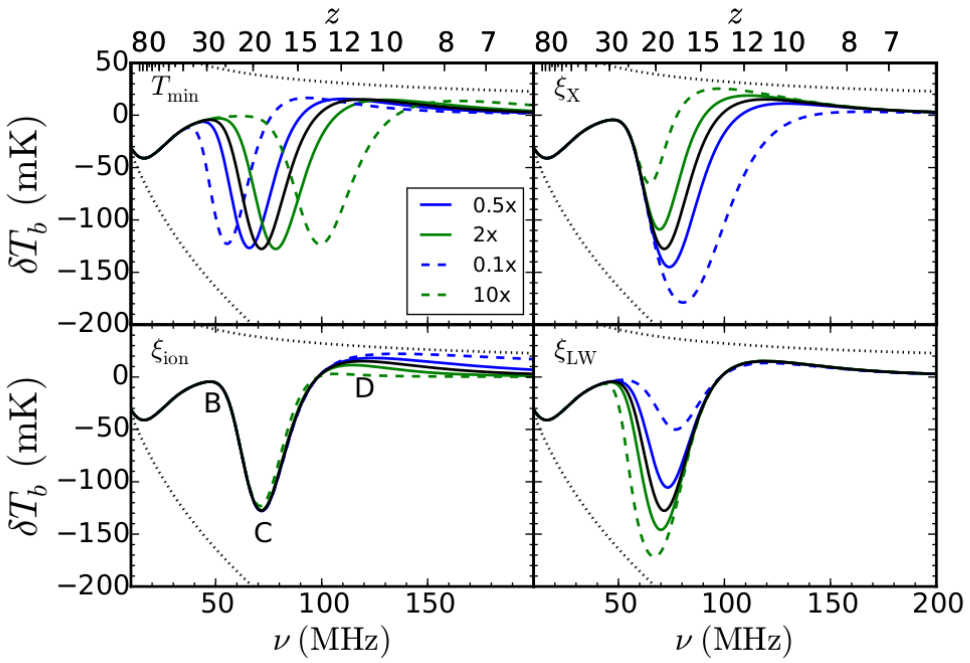

FIGURE 1.7: Illustration of the basic dependencies of the global 21-cm signal. The black line is the same in each panel, representing the reference model, while all solid green (blue) lines correspond to a factor of 2 increase (decrease) in the parameter noted in the upper left corner, and dashed lines are factor of 10 changes above and below the reference value (from Mirocha et al., 2015).

1.2 Current constraints on the global 21-cm signal

The most stringent upper limits on the global 21-cm signal in the $6 < z < 12$ range (when reionization is expected to happen) are set by the EDGES and SARAS experiments.

Monsalve et al. (2017) constrained the duration of reionization to be $\Delta z > 1.3$ for a reionization redshift $z_r = 8.5$. If the assumption that the gas is heated well above the CMB before widespread reionization begins is relaxed, the EDGES results constrain a "cold reionization" scenario at $z_r = 6$ ($\Delta z < 2$) with a mean Hydrogen neutral fraction to $x_{HI} < 1\%$ at redshift z = 6. Similar constraints on cold reionization are obtained from SARAS observations that rule out models of inefficient heating ($\xi_X \leq 0.1$) if reionization occurs rapidly (Singh et al., 2017).

SCI-HI and LEDA target the signal at higher redshifts ($z > 13$). Voytek et al. (2014) report a 1 K rms upper limit in the $14.8 < z < 22.7$ range, whereas Bernardi et al. (2016) set a 95% confidence level of 890 mK on the amplitude of the 21-cm signal in the $13.2 < z < 27.4$ range ($100 > \nu > 50$ MHz).

Recently, Bowman et al. (2018) reported the first detection of the 21-cm global signal as an absorption profile centred at 78 MHz. Figure 1.8 shows the spectrum measured in the $50 - 100$ MHz range, together with the best fit cosmological 21-cm model and the residual spectrum obtained after subtracting the best fit foreground and cosmological models respectively. The best-fit to the 21-cm signal yielded a symmetric absorption profile centred at 78 ± 1 MHz ($z \sim 17$), with a brightness temperature $T_b = -500^{+500}_{-200}$ mK (see the thick black line (H2) in Figure 1.9). Such amplitude is brighter than the most optimistic model and has called for an exotic interpretation in terms of collisional dark matter, i.e. the observed profile amplitude can be explained if the baryons loose energy through collisions with the colder dark matter (Barkana, 2018).

Hills et al. (2018) re-analyzed the EDGES data and found inconsistent results, choosing the same frequency range, in particular unphysical best fit values for some fo the foreground parameters. Both the re-analysis by Hills et al. (2018) and the ad hoc theoretical models required to explain the signal call for an independent confirmation of the measurement.

The remaining of the thesis is organized as follows:

- Chapter 2 presents a description of foregrounds of Galactic and extra galactic origins, and the challenges they introduce to the global 21-cm observations, their mitigation techniques and the motivation for this work;
- Chapter 3 describes the simulations of foreground spectra as observed by a realistic 21-cm global signal experiment. We describe the two foreground templates used, i.e. the 408 MHz Haslam et al. (1982) and Remazeilles et al. (2015) all-sky maps, and the single dipole used. We also describe how the foreground spectra were modeled;

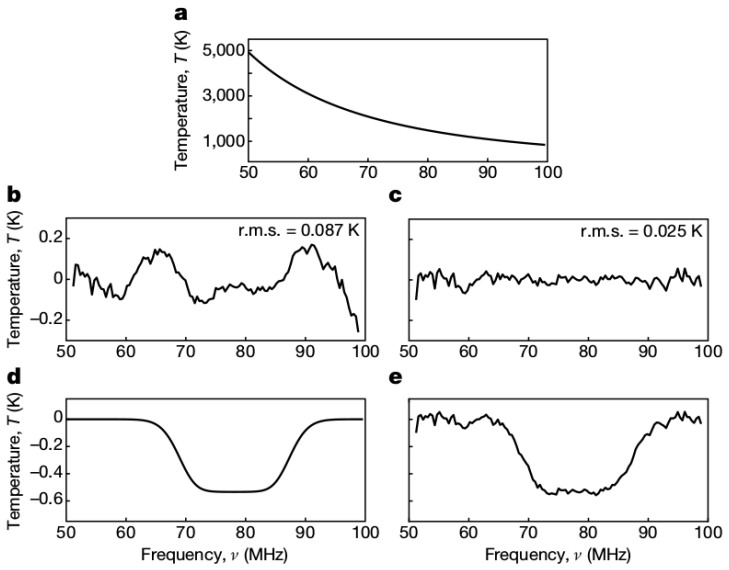

FIGURE 1.8: From top to bottom: (a) measured EDGES spectrum; residual spectra obtained after fitting and subtracting: (b) the foreground model (c) both the foreground and 21-cm models; (d) best fitting 21-cm model; (e) sum of (d) and (c) spectra (from Bowman et al., 2018).

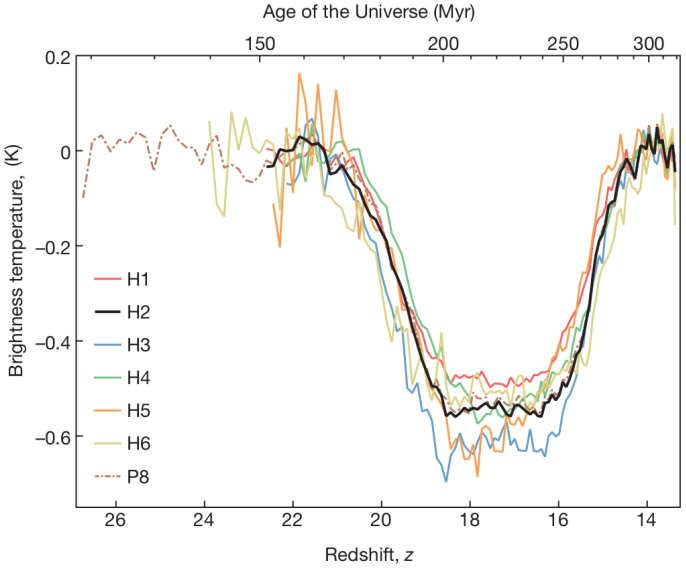

FIGURE 1.9: The resported EDGES absorption trough. The thick black curve represents the model with the highest signal to noise ratio (from Bowman et al., 2018).

- conclusions are drawn in Chapter 4.

Chapter 2

Foreground overview

Observations of the redshifted 21-cm signal from EoR are contaminated by strong astrophysical foregrounds (i.e., Furlanetto et al., 2006; Santos et al., 2005), ionospheric distortions and non-ideal instrumental response. Foregrounds can either be of Galactic or extagalactic nature (see Figure 2.1) and understanding their properties is essential in order to separate them from the 21-cm signal (Bowman et al., 2009; Dillon et al., 2014; Jelić et al., 2010; Kerrigan et al., 2018; Liu & Tegmark, 2011; Morales et al., 2006; Parsons et al., 2010; Pober et al., 2016; Santos et al., 2005; Trott et al., 2016; Vedantham et al., 2012; Wang et al., 2013, 2006). In the next sections I will give a brief overview of the foreground characteristics.

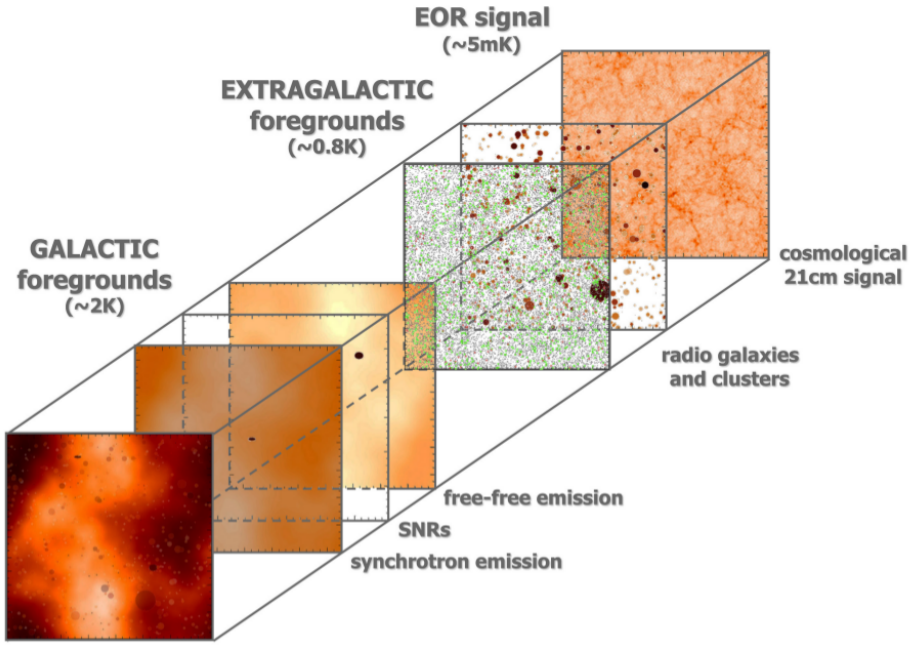

FIGURE 2.1: Cartoon representation of the various foreground components superimposed to the 21-cm signal (from Zaroubi, 2012).

2.1 Galactic Synchrotron Emission

Galactic synchotron emission results from the relativistic electron accelerated in a magnetic field (He, 2009) and is the brightest foreground at frequency below 1 GHz (e.g., de Oliveira-Costa et al., 2008). Its intensity as a function of frequency $I(\nu)$ can be written as (Jelić et al., 2008):

$$I(\nu) \propto N_e B_{\perp}^{(\gamma+1)/2} \nu^{\alpha}, \tag{2.1}$$

where N_e is the electron number density, $B_{\perp}$ the Galactic magnetic field component perpendicular to the line of sight, while γ is the power law index of the electron spectral energy distribution and $\alpha = -(\gamma - 1)/2$ is the spectral index in flux density units. Converting the flux density units to brightness temperature T_b, the power law relationship can be re-written as:

$$T_b(\nu) \propto \nu^{\beta}, \tag{2.2}$$

with $\beta = -2 + \alpha$.

At frequencies below 1 GHz, the 408 MHz map by Haslam et al. (1982) at ~ 51 arcmin resolution and its improved version by Remazeilles et al. (2015) best describe the Galactic synchrotron emission. Beuermann et al. (1985) modelled the emission at 408 MHz as the combination of two components: a thin disk that essentially corresponds to the gaseous disk and a thick disk that extends from 2 kpc at $R = 5$ kpc up to 6 kpc at $R = 15$ kpc ($R_0 \sim 8.5$ kpc is the distance of the Sun from the Galactic centre, Beuermann et al., 1985). The thick (thin) disk constitutes the diffuse synchotron emission of the galaxy and contributes to 90% (10%) of the total emission (Beuermann et al., 1985). The emission of the thin disk results from the superposition of non thermal emissions from unresolved supernova remnants (Caswell & Lerche, 1979; Ilovaisky & Lequeux, 1972) and thermal emission from extend low-density H II regions (Güsten & Mezger, 1982; Mezger & Pauls, 1979).

At 408 MHz the overall power of the galaxy is $\sim 9 \times 10^{21}$ W Hz^{-1}, with the radio emission extending to $R \gtrsim 16$ kpc. Emission contours of the two components are shown in Figure 2.2. Observations performed with the 22 MHz radio telescope at the Dominion Radio Astrophysical Observatory (DRAO) resulted in maps of the radio emission between declinations $-28°$ and $+80°$, covering $\sim 73\%$ of the sky (Roger et al., 1999). The derived map shows the large scale features of the galactic emission which include the North Polar Spur, the thick non-thermal disk, and absorption due to discrete H II regions and to an extended band of thermal electrons within $40°$ of the galactic centre.

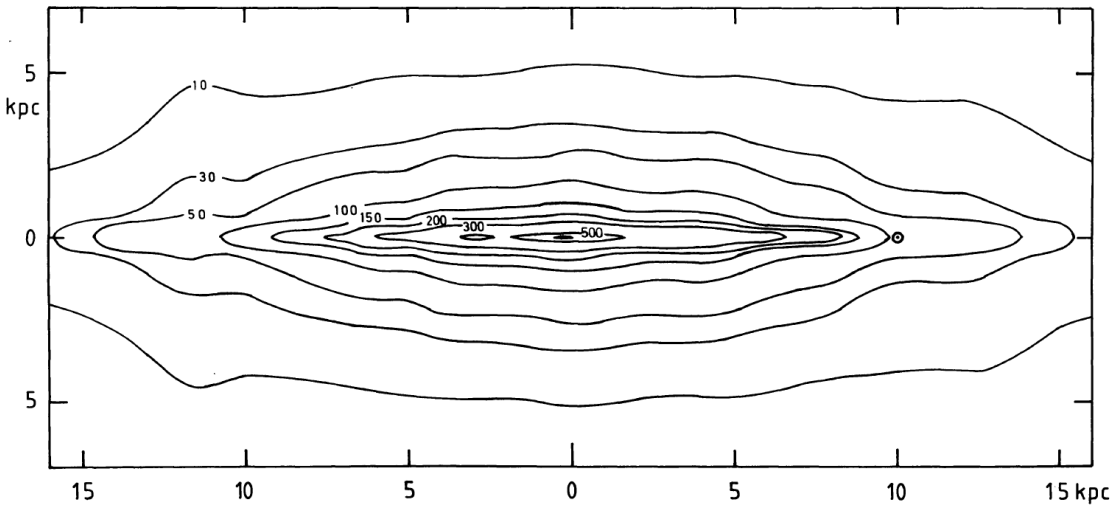

FIGURE 2.2: Radio contours (Kelvin units) of the Galactic emission at 408 MHz seen at $l = 90°$, showing the total emission from both the thin and thick disk (from Beuermann et al., 1985).

A comparison made between the 22 MHz and 408 MHz maps shows a remarkable constancy of spectral index in the extended emission corresponding to the thick disk component over the full range of longitudes from $\sim 0°$ to $\sim 240°$, with a steepening at high Galactic latitudes (Roger et al., 1999).

At frequencies below 200 MHz, observations of Galactic emission have an angular resolution poorer than the Haslam map and the spectral index can only be measured over large patches of sky. The spectral index of the synchrotron emission between 408 MHz and 23 GHz is $\beta \sim -2.5$ at low Galactic latitudes, steepening towards the poles ($\beta \sim -3.0$, Bennett et al., 2003).

Recent observations in the $100 - 200$ MHz range also indicate that Galactic emission has a spectral index $\beta \sim -2.6$ between 100 and 408 MHz (Mozdzen et al., 2017; Patra et al., 2015; Rogers & Bowman, 2008) with a flattening $\beta \sim -2.4$ towards the Galactic plane (Mozdzen et al., 2017).

2.2 Extragalactic Foregrounds

Extragalactic foreground emission results from extragalactic radio sources. The radio emission from the brightest radio sources is due to the accretion on massive black holes at the centers of galaxies (Gleser et al., 2008), whereas at sub-mJy flux densities the contribution of star formation becomes important (Jelić et al., 2008; Sadler et al., 2002).

Most extragalactic sources show a power law spectrum, with a median spectral index $\langle \alpha \rangle = -0.8$ (De Breuck et al., 2000), although some sources show a turnover at low

frequencies that is consistent with synchrotron self-absorption (Callingham et al., 2017). From the integrated source counts, extragalactic radio sources contribute up to 30% of the total foreground power (e.g., Bridle & Baldwin, 1967).

2.3 Foreground subtraction in global 21-cm observations and thesis motivation

In global signal observations, the 21-cm signal is extracted using the frequency information alone and phenomenological models are often used to describe both the foregrounds and the 21-cm signal (Shaver et al., 1999). A popular parameterization used for the foreground spectrum is a log-polynomial expansion in frequency (Bernardi et al., 2015; Bowman & Rogers, 2010; Voytek et al., 2014) and a slowly declining function like an inverse hyperbolic tangent for the 21-cm signal during reionization (Bowman & Rogers, 2010) and a Gaussian absorption trough for the dark age 21-cm signal (Bernardi et al., 2016).

Single-dipole observations measure the integrated Galactic foreground spectrum averaged over a large sky area, losing information about its spatial structure: this may lead to mix spatial into spectral foreground structure, effectively exacerbating the separation problem (Bernardi et al., 2015). Liu et al. (2013) suggested that the spatial structure of the Galactic foreground can be used - if accurately known - in order to minimize the mixing between spatial and spectral modes and, eventually, improve its separation from the spatially-constant 21-cm signal. The goal of this thesis is to test this assumption by performing realistic simulations of foreground spectra as observed by 21-cm global signal experiments. In the next section I will describe the ingredients of the simulations (a realistic dipole beam and two templates that differ in the small angular scale structure) and how the simulated foreground spectra are obtained.

Chapter 3

Simulated foreground observations

In this section we carry out the simulations of foreground spectra as observed by a 21-cm global signal experiment, including a realistic instrument. We will simulate the instrument by modeling the antenna beam as a function of frequency and also using a reference ideal beam. We will carry out two simulations with different input foregrounds and compare the simulated spectra by fitting a parametric foreground model.

3.1 Formalism

At a time t, an individual antenna can measure its beam weighted sky brightness temperature T_{ab} at a pointing direction $\hat{n}$ as (Bernardi et al., 2015):

$$T_{ab}(t,\nu,\hat{n}) = T_N(t,\nu) + \left(\int_\Omega A_{\hat{n}}(\nu,\hat{n}')d\hat{n}'\right)^{-1} \times \left[\int_\Omega T_{sky}(t,\nu,\hat{n}')A_{\hat{n}}(\nu,\hat{n}')d\hat{n}'\right] g(t,\nu), \tag{3.1}$$

where ν is the frequency of observation, T_{sky} is the direction dependent sky brightness temperature of the entire sky Ω, whiles $A_{\hat{n}}(\nu,\hat{n}')$ is the antenna gain pattern in the direction $\hat{n}'$ and $g(t,\nu)$ is the overall receiver gain. Assuming an ideal ($g = 1$) and noiseless instrument ($T_N = 0$), $T_{ab}(t,\nu,\hat{n})$ becomes:

$$T_{ab}(t,\nu,\hat{n}) = \left(\int_\Omega A_{\hat{n}}(\nu,\hat{n}')d\hat{n}'\right)^{-1} \times \left[\int_\Omega T_{sky}(t,\nu,\hat{n}')A_{\hat{n}}(\nu,\hat{n}')d\hat{n}'\right], \tag{3.2}$$

which can further be decomposed into the foreground $T_f(t, \nu, \hat{n})$ and 21-cm signal component $T_{HI}(\nu)$ (Bernardi et al., 2015; Morandi & Barkana, 2012) as:

$$T_{ab}(t, \nu, \hat{n}) = T_f(t, \nu, \hat{n}) + T_{HI}(\nu), \tag{3.3}$$

with different dependencies on time, frequency and positions. The foreground spectrum can be modeled as $\hat{T}_f$ (Bernardi et al., 2015; Bowman & Rogers, 2010; Harker, 2012):

$$\log \hat{T}_f(\nu) = \sum_{n=0}^{m} c_n \log(\nu)^n. \tag{3.4}$$

The residual spectrum $T_r(\nu)$, obtained after subtracting $\hat{T}_f(\nu)$ from $T_f(\nu)$ is defined as:

$$T_r(\nu) = T_f(\nu) - \hat{T}_f(\nu) \tag{3.5}$$

The goodness of fit of the foreground spectrum will be quantified using the root mean square of the residual spectrum RMS, RMS_r :

$$RMS_r = \sqrt{\left\langle \left(T_f(\nu) - \hat{T}_f(\nu)\right)^2 \right\rangle}, \tag{3.6}$$

where the angle bracket $\langle ... \rangle$ is the average over frequency.

3.2 Input foreground templates

Two different foreground templates were used for our simulation. The first is the already mentioned Haslam et al. (1982) at 408 MHz. The second is a re-analysis of the Haslam et al. (1982) map carried out by Remazeilles et al. (2015) where some of the artifacts left in the original map have been mitigated. In particular the amplitude of the stripes present in the Haslam et al. (1982) was reduced by using a Fourier-based filtering technique (Figure 3.1). The reprocessed map also has sources brighter than 2 Jy removed, using a combination of a two-dimensional Gaussian fitting and minimum curvature spline surface inpainting. Eventually, the Haslam et al. (1982) and Remazeilles et al. (2015) maps have spatial differences on scales up to a few degrees due to both the removal of point sources and image artifacts. Our simulations will quantify the impact of these differences on the foreground spectrum.

In order to extrapolate our 408 MHz synchrotron templates to the $100-200$ MHz range, we derived an all-sky spectral index map $\beta(\hat{n})$. Our goal is not to generate the most accurate spectral index map but a reasonably realistic one and, in order to do so, we used the Haslam map $T_{408}(\hat{n})$ (Figure 3.2) and the 150 MHz map $T_{150}(\hat{n})$ obtained by

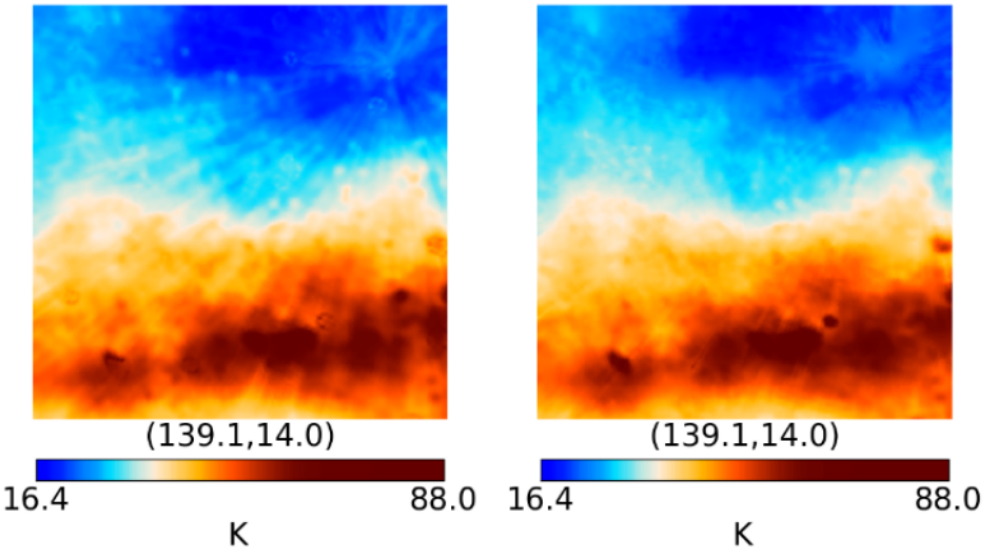

FIGURE 3.1: A 33°× 33° gnomonic projection of the 408 MHz Haslam map centered at Galactic coordinates (l,b)= (139°, 14°), near the north celestial pole. The left panel displays the striped map (Haslam et al., 1982) while the right shows the newly destriped map (from Remazeilles et al., 2015).

the Global Sky Model (de Oliveira-Costa et al., 2008). de Oliveira-Costa et al. (2008) used sky maps in the $0.01-94$ GHz range to determine their spectral behaviour through a principal component analysis. In this way, an all sky map can be generated at any given frequency[1].

The all-sky spectral index map $\beta(\hat{n})$ is calculated as:

$$\beta(\hat{n}) = \frac{\ln \frac{T_{408}(\hat{n})}{T_{150}(\hat{n})}}{\ln \frac{408}{150}}. \tag{3.7}$$

The resulting spectral index map is shown in Figure 3.3. Foreground maps at any frequency ν can then be obtained from the scaled Haslam and Remazeilles (T_{rem}) maps as:

$$\begin{aligned} T_*(\nu,\hat{n}) &= T_{408}(\hat{n})\left(\frac{\nu}{\nu_{408}}\right)^{\beta(\hat{n})} \\ T_{**}(\nu,\hat{n}) &= T_{rem}(\hat{n})\left(\frac{\nu}{\nu_{408}}\right)^{\beta(\hat{n})}, \end{aligned} \tag{3.8}$$

where T_* (T_{**}) indicates the scaled Haslam (Remazeilles) template. xample of $T_*(\nu,\hat{n})$ is shown in Figure 3.4.

[1]We use the Python implementation of the GSM, PyGMS: https://github.com/telegraphic/pygsm

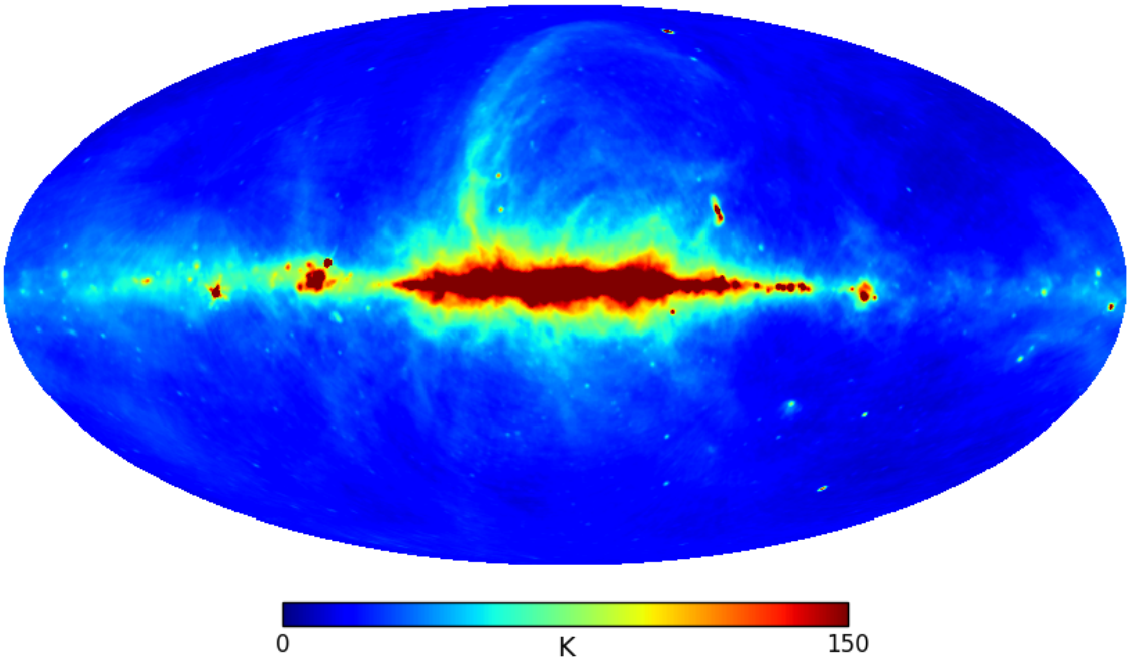

FIGURE 3.2: The 408 MHz map of the diffuse Galactic radio emission (from the PyGSM package).

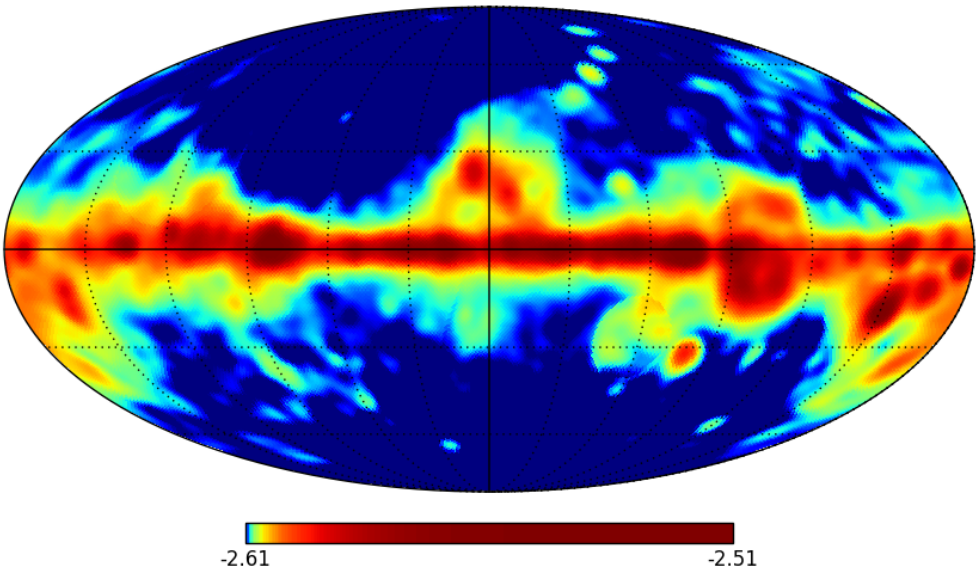

FIGURE 3.3: The spectral index map $\beta(\hat{n})$ pixelized in the Healpix frame with nside = 512 (Górski et al., 2005). The spectra index flattens in the Galactic plane and steepens away from the plane.

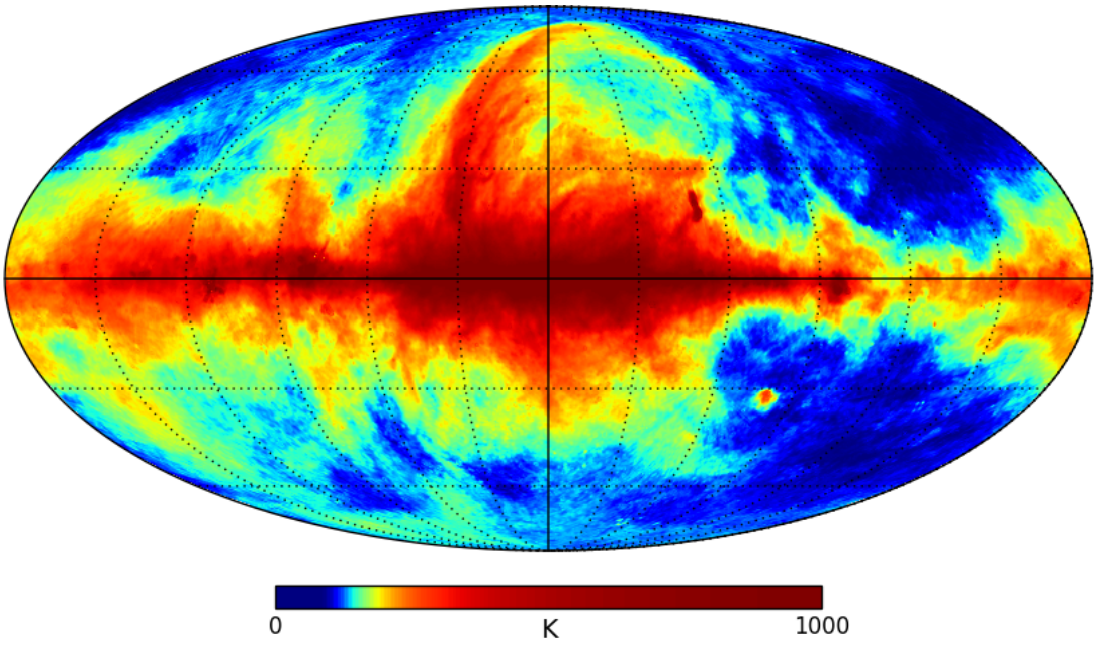

FIGURE 3.4: A mollweide projection of the Haslam map simulated at 200 MHz.

3.3 Observation simulations

In this section, we simulate a 21-cm global signal observation assuming that the experiment is located at the Karoo reserve area in South Africa ($-30°$ latitude). Our simulations essentially follow the procedure described in Bernardi et al. (2015).

Our final goal is to generate foreground spectra in the $100-200$ MHz range with 1 MHz separation. In order to do so, we use the PAPER beam model described in Nunhokee et al. (2017). Figure 3.5 shows a single dipole antenna of PAPER, while Figure 3.6 shows the simulated beam model at 100, 150 and 200 MHz, with the relative difference between frequencies shown in Figure 3.7). The beam simulations are carried out 10 MHz apart and at a fixed grid of spatial points (for further details, see Nunhokee et al., 2017). In order to obtain a beam model at any intermediate frequency ν_{int} and direction $\hat{n}$, we interpolated in both the frequency and spatial direction. Along the frequency direction we performed a weighted linear interpolation between the two closest beam models g (Nunhokee et al., 2017):

$$g'(\hat{n}, \nu_{int}) = \frac{w_a\, g_a(\hat{n}, \nu_a) + w_b\, g_b(\hat{n}, \nu_b)}{w_a + w_b}, \tag{3.9}$$

where the weights w_i with $i = a, b$ are taken as:

$$w_i = \frac{1}{|\nu_{int} - \nu_i|}. \tag{3.10}$$

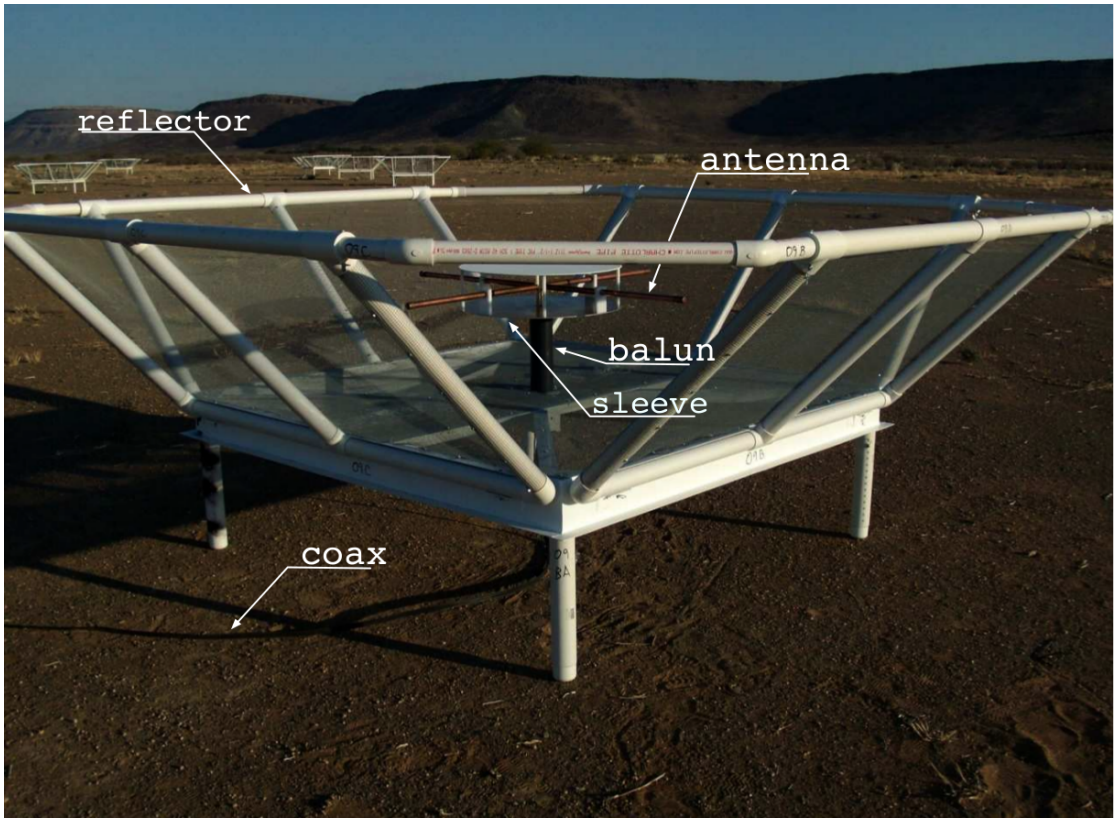

FIGURE 3.5: A PAPER dipole instrument at Karoo desert in South Africa. Image credit: http://eor.berkeley.edu/.

Furthermore, since our sky model is pixelized in the healpix frame, we need to spatially interpolate our beam model on the Healpix grid. This was obtained by a weighted linear interpolation of the three points closest to Healpix pixel $\hat{n}_{int}$ specified by the equatorial coordinates $(\alpha_{int}, \delta_{int})$:

$$\hat{g}(\hat{n}_{int}, \nu_{int}) = \frac{v_a\, g'_a(\hat{n}_a, \nu_{int}) + v_b\, g'_b(\hat{n}_b, \nu_{int}) + v_c\, g'_c(\hat{n}_c, \nu_{int})}{v_a + v_b + v_c}, \tag{3.11}$$

and the weights v_i with $i = a', b', c'$ are taken as:

$$v_i = \frac{1}{\sqrt{(\alpha_{int} - \alpha_i)^2 + (\delta_{int} - \delta_i)^2}}, \tag{3.12}$$

The simulated observation with T_* and T_{**} as a function of time t, frequency ν and direction $\hat{n}$ becomes $T'_*(t, \nu, \hat{n})$ and $T'_{**}(t, \nu, \hat{n})$ respectively,

$$T'_*(t, \nu, \hat{n}) = T_*(t, \nu, \hat{n})\, \hat{g}(\nu, \hat{n}), \tag{3.13}$$

$$T'_{**}(t, \nu, \hat{n}) = T_{**}(t, \nu, \hat{n})\, \hat{g}(\nu, \hat{n}). \tag{3.14}$$

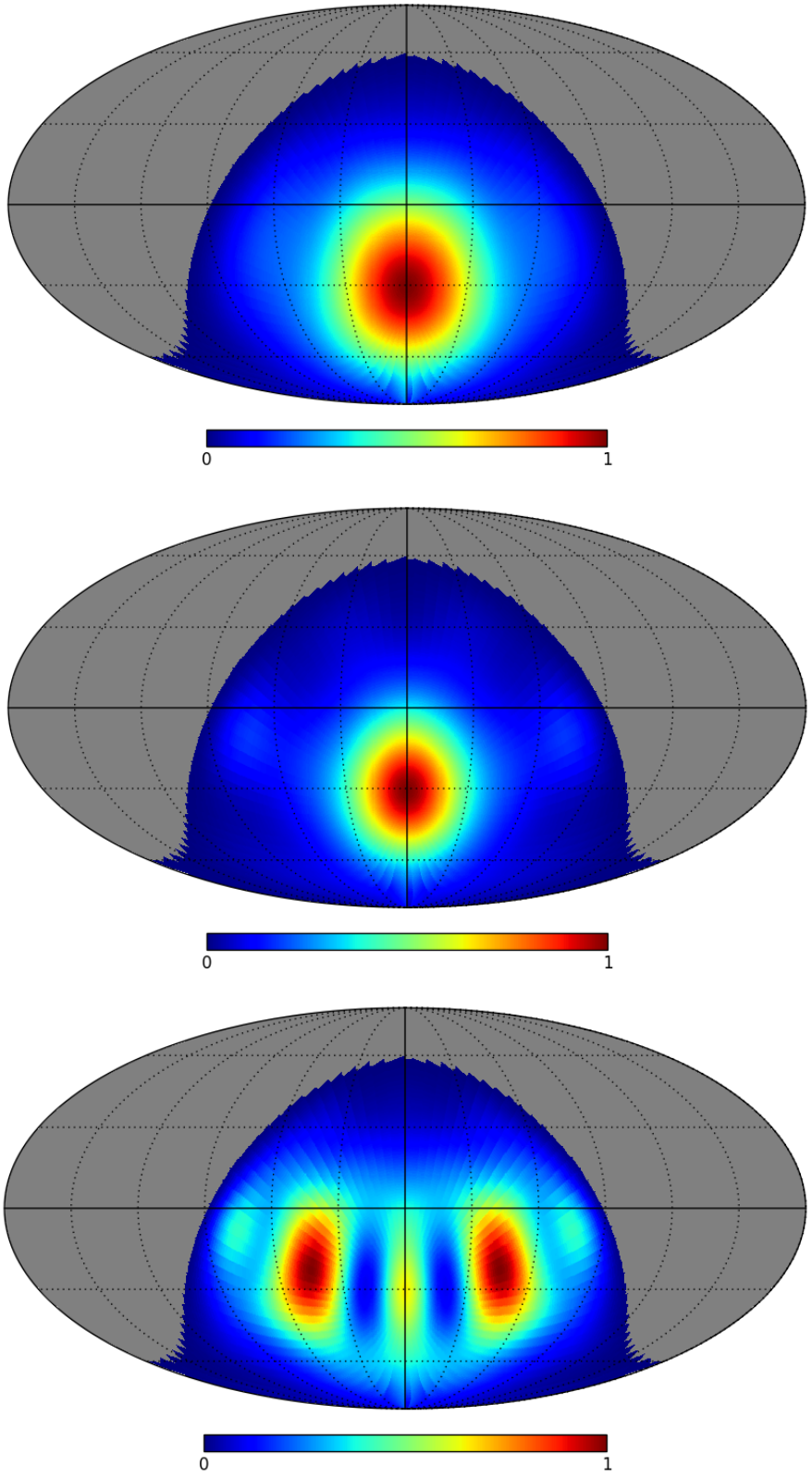

FIGURE 3.6: PAPER beam model at 100 (top), 150 (middle) and 200 MHz (bottom) respectively. The simulation at high frequencies shows side lobes that appear even brighter than the main lobe and these beam models likely impose extra spectral structure once they are multiplied with the foreground model. The region below the horizon is in grey.

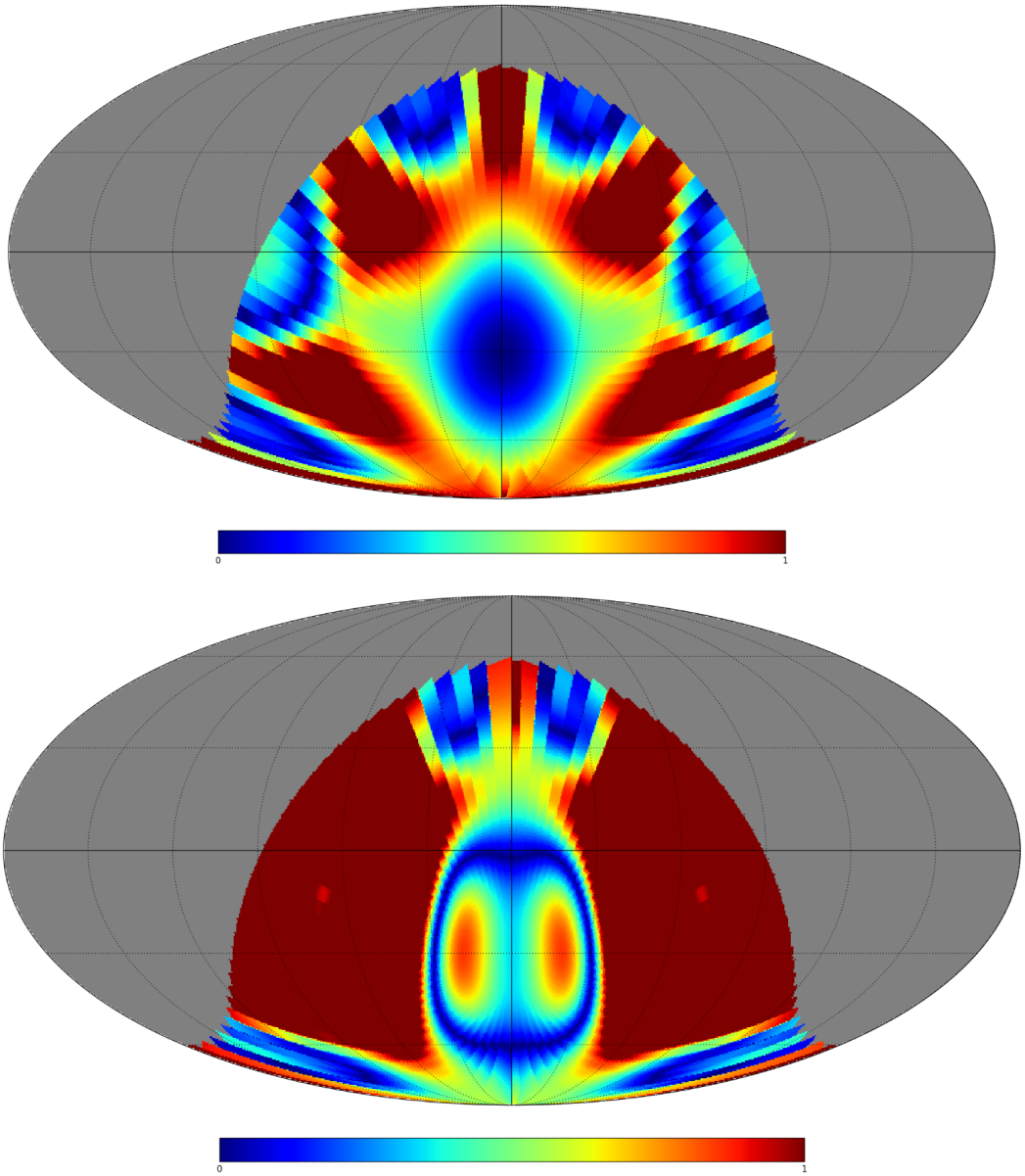

FIGURE 3.7: Relative difference between the PAPER beam model at 150 MHz and 100 MHz (top) and at 150 MHz and 200 MHz (bottom) pixelized in the Healpix frame (Górski et al., 2005). We notice the significant difference between the simulations at 150 and 200 MHz. We do not investigate the origin of such discrepancy although we realize that it is likely to create artificial additional structure in the simulated spectra.

Examples of $T'_{**}(t, \nu, \hat{n})$ are displayed in Figure 3.8.

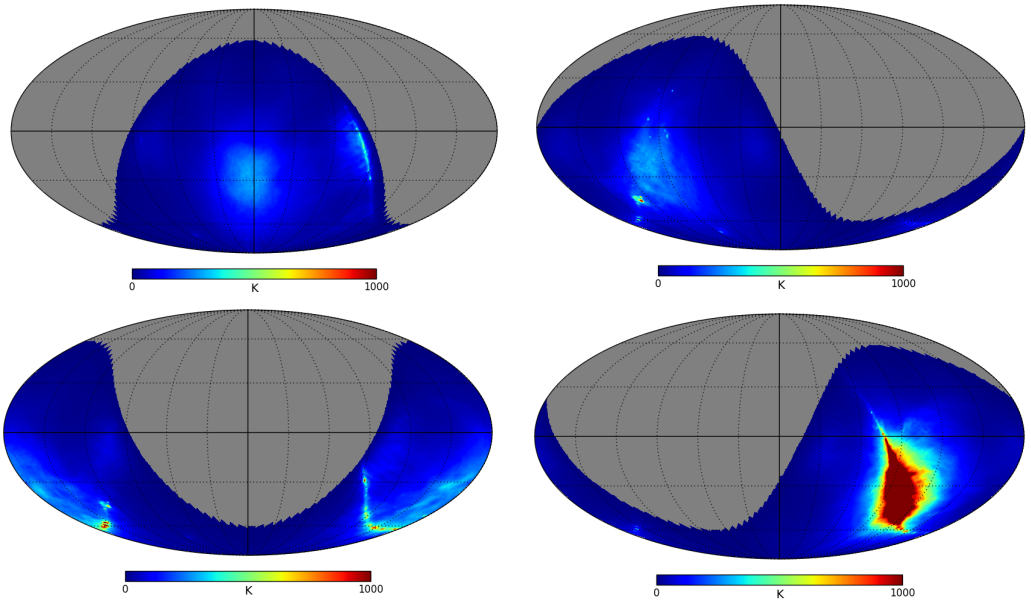

FIGURE 3.8: Simulated observation $T'_{**}(t, \nu, \hat{n})$ (i.e., the Remazeilles template), of the Southern sky at a frequency of 150 MHz observed at LSTs 0 (Top left), 6 (Top right), 12 (Bottom left) and 17 hours (Bottom right). The coldest sky patches occurs at 8 < LST < 0 hrs, when the Galactic centre is attenuated by the horizon response of the PAPER dipole. As expected, the brightest sky patch is at LST 17 hrs, when the Galactic plane drifts overhead.

3.4 Simulated spectra

In this section we generate the spectrum $T_{f,j}(\nu)$, over LSTs 0-9 hours as:

$$T_{f,j}(\nu) = \left\langle \left(\int_{\Omega} \hat{g}(\nu, \hat{n}) d\hat{n} \right)^{-1} \left[\int_{\Omega} T'_j(t, \nu, \hat{n}) d\hat{n} \right] \right\rangle_t, \tag{3.15}$$

where T'_j is the simulated observation described in Section 3.3 with $j = *$ or $**$, $\hat{g}(\nu, \hat{n})$ spatial and frequency interpolated beam and $\langle ... \rangle_t$ is the average over time. We also included an ideal case where we used the Haslam map with $\hat{g}(\nu, \hat{n}) = 1$, i.e. an ideal beam whose response is constant with frequency and direction in the sky, in order to test our simulation procedure against results already obtained in the literature (e.g., Bernardi et al., 2015; Pritchard & Loeb, 2010). Each spectrum is then modelled as a polynomial in $\log \nu$ (equation 3.4). The resulting spectra generated for our three cases (Haslam with ideal beam, Haslam and Remazeilles template) together with their best fit are displayed in Figure 3.9. Residual spectra after subtracting polynomials of increasing orders (equation 3.5) are displayed in Figure 3.10, 3.11 and 3.12.

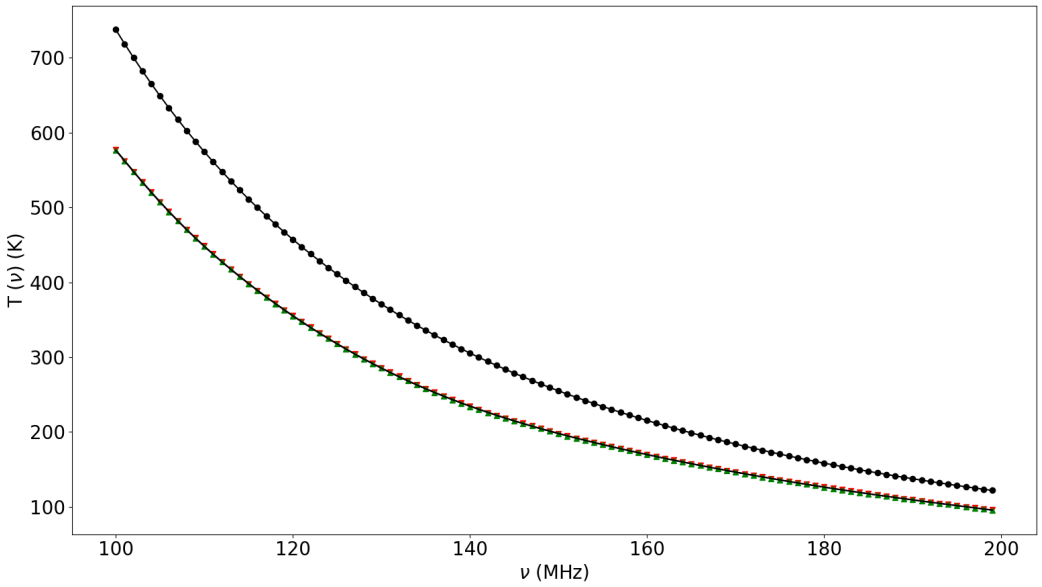

FIGURE 3.9: The foreground spectrum derived from the Haslam map (black dots) in the case of an ideal dipole beam response (i.e., $\hat{g}(\nu, \hat{n}) = 1$), the Haslam (red triangle) and the Remazeilles (green triangle) templates with the PAPER beam and their polynomial best fit models (solid line).

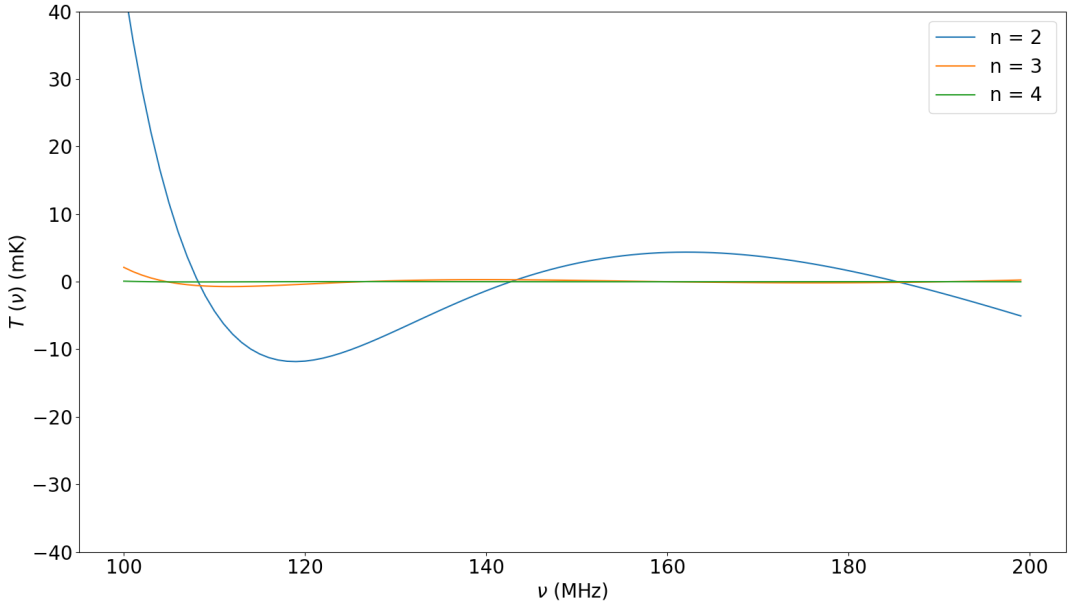

FIGURE 3.10: Residual spectra obtained after fitting polynomials with increasing order to the idealized spectrum case (Figure 3.9). Residuals decrease very quickly, approaching zero already for the 4^{th} order polynomial.

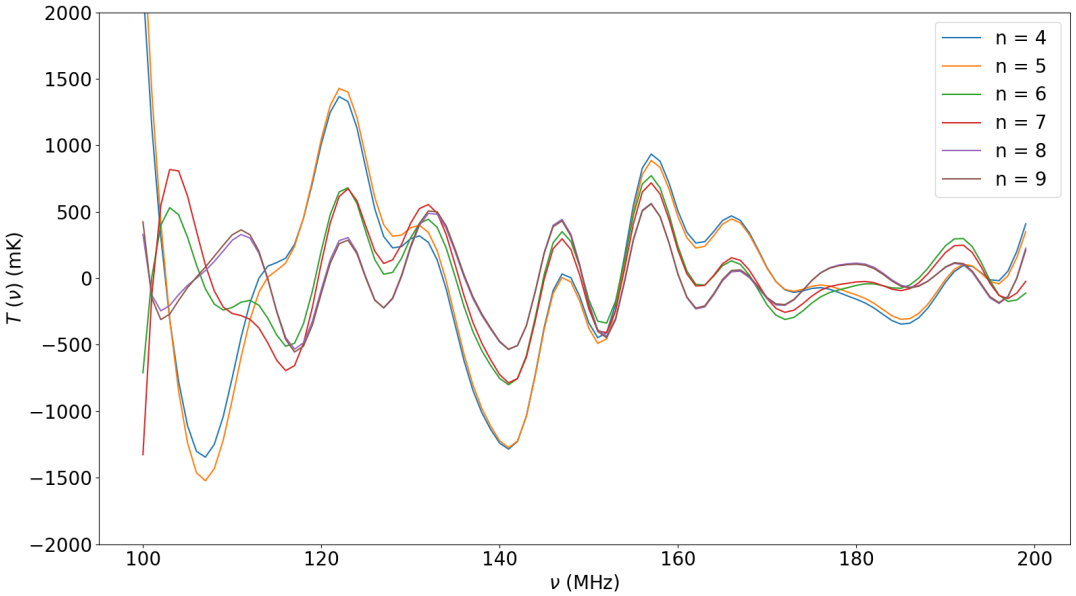

FIGURE 3.11: Same as Figure 3.10 but for the Haslam map convolved with the dipole beam. We note that residuals do not approach zero even after fitting an $n = 9$ order polynomial.

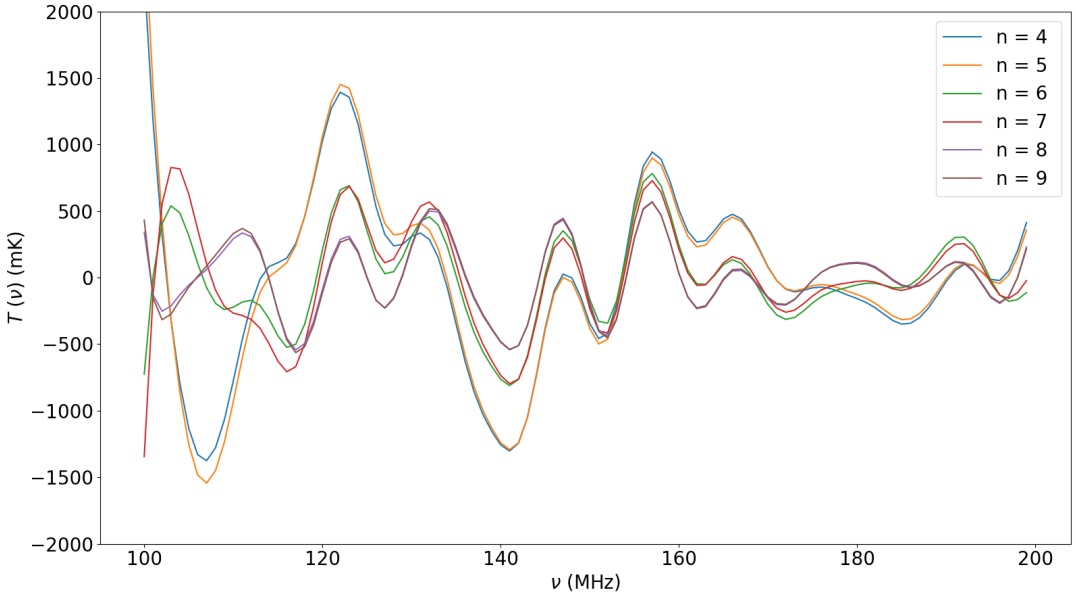

FIGURE 3.12: Same as Figure 3.11, but with the Remazeilles map.

Remezeilles templates) an additional orders for foreground subtraction is required, this can be visualized in Figures 3.11 and 3.12 where even after the ninth order polynomial fit the residual spectrum RMS remained at $\backsim$ 300 mK, while the cosmological signal in most models is at best 30 mK This means, the generated residual spectra is 1 order of magnitude brighter than the theoritically predicted value, and thus the incorporation of the beam response (i.e the interpolated beam in frequency) may have introduced structures in frequency that may not be modeled by the polynomial function, and the implementation of the parametric foreground subtraction method may not be the best approach to be used for this work. Significance of the residuals were quantified through their RMS (equation 3.6).

We note that, in the ideal case, the foreground spectrum can be fitted very well by a low order polynomial and, for a 4^{th} order, residuals are already well below 1 mK (Figure 3.13). This is consistent with previous findings in the literature and a confirmation that, in the case of an idealize beam, the foreground spectrum appears very smooth.

Conversely, residuals remain high for both the simulations where the realistic dipole beam was used. Even after a fit with a 9^{th} order polynomial, their residual RMS remains at the $\sim$ 250 mK, i.e. an order of magnitude higher than the peak of the 21-cm signal (Figure 3.14). Figure 3.15 shows, however, that the relative difference ϕ between the RMS of the two simulations remains small up to the maximum polynomial order used, where

$$\varphi = \frac{RMS_{*} - RMS_{**}}{RMS_{*}} \times 100. \tag{3.16}$$

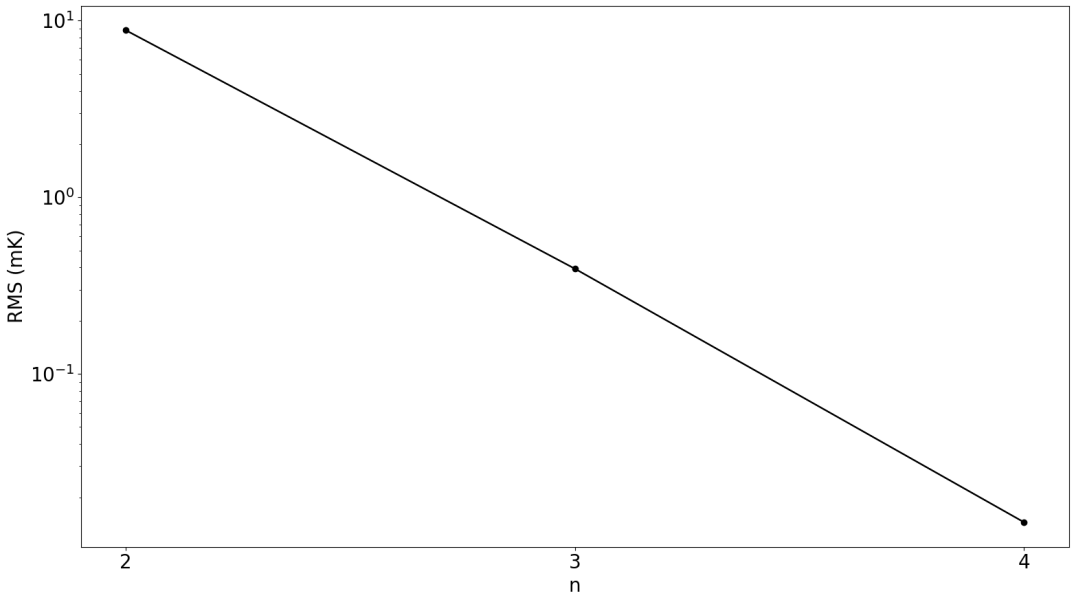

FIGURE 3.13: Residual RMS as a function of polynomial order for the spectrum obtained from the Haslam map with the idealized dipole response (Figure 3.9). A low order foreground fits the spectrum very well.

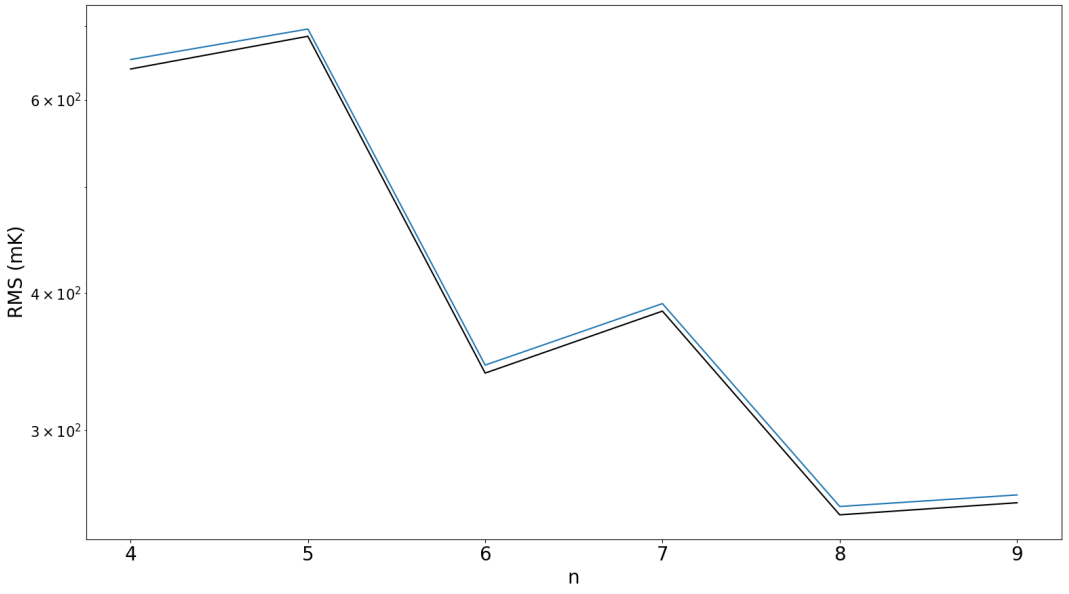

FIGURE 3.14: The residual RMS spectrum for both the Haslam and Remazeilles templates on the same plot shows no significant difference.

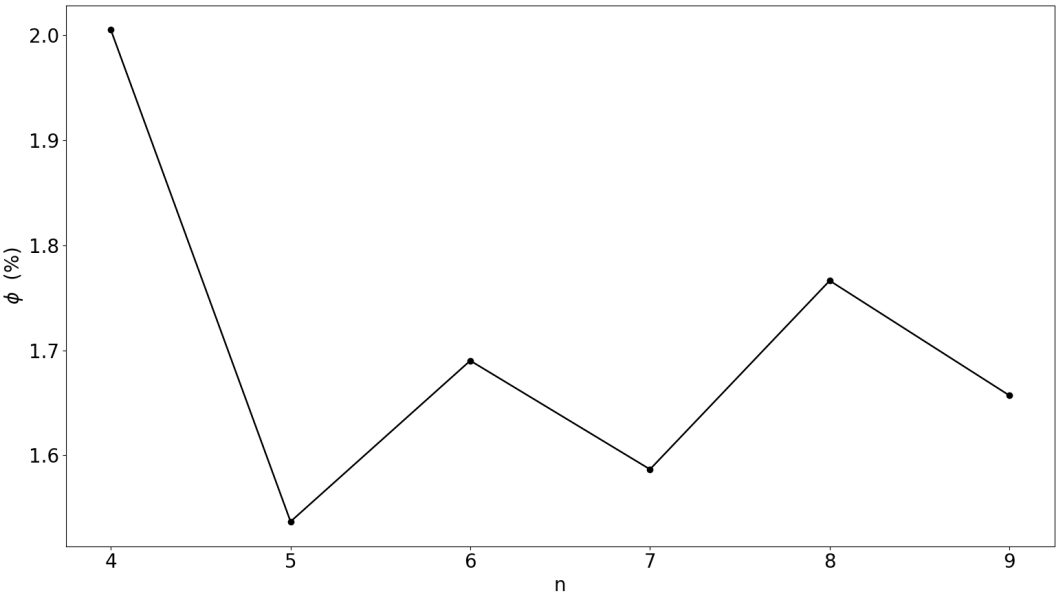

FIGURE 3.15: The relative difference in the residual spectrum RMS ϕ as a function of polynomial order. Both RMS profiles remain relatively flat beyond $n = 6$, with an average percentage value of 1.7.

Conclusion and Future Works

One of the frontiers in modern cosmology is to understand when and how the first luminous structures formed in our Universe, how they evolved and, subsequently, how they ionized the IGM. As observations of the redshifted 21-cm line directly probe the evolution of the IGM and they can best address these questions. The first detection of the cosmological sky-averaged 21-cm line has been recently reported (Bowman et al., 2018). The main obstacle to 21-cm measurements are foregrounds: they are a few orders of magnitude brighter than the 21-cm signal everywhere in the sky and the only possibility to separate the two signals is to leverage on their different spectral properties.

In this thesis the spectral properties of Galactic foregrounds were investigated through simulations of realistic observations of the sky-averaged 21-cm signal. In particular we investigated the impact of small scale structure on the simulated foreground spectra.

We used the Haslam et al. (1982) and its improved version where point sources and some of the scanning artifacts were subtracted (Remazeilles et al., 2015) as foreground templates. We extrapolated them in the $100 - 200$ MHz frequency range and generated foreground spectra by convolving them with a realistic model of a dipole antenna. For comparison we also generated a simulated spectrum without including the dipole response.

Each spectra was then modeled as a polynomial expansion in $\log \nu$ and residuals quantified through their root mean square - RMS. We found that a third order polynomial can be used to model foregrounds in the ideal case (i.e without coupling the antenna response to them), in agreement with previous works (Bernardi et al., 2015; Pritchard & Loeb, 2010).

Once a dipole beam is used, we found that the simulated spectra are overall not well fitted using a log-polynomial expansion as a basis function. Even after a ninth order polynomial fit, the residual spectrum RMS remained at the level of $\lesssim 250$ mK, whereas the cosmological signal is anticipated to be ~ 30 mK at best. We note that our simulated dipole changes its spatial structure noticeably across the frequency range considered (see,

for example, Figure 3.7) and we cannot exclude that (part of) the spectral structure is artificially introduced by our simulations or our interpolation scheme. The residual spectral structure is, however, similar in both simulated cases, i.e. using the Haslam et al. (1982) and Remazeilles et al. (2015) maps. Their relative difference in RMS values is below 2% up to the ninth order polynomial. This value leads to an absolute difference in residual spectra between the two foreground models up to ~ 5 mK, which is $\sim 20\%$ of the peak 21-cm signal. From our analysis we can conclude that differences in the small scale structure of foregrounds have a limited impact on the observed foreground spectra and similiar (within 2%) residual RMS values can be obtained if they are modeled with log-polynomials.

We notice, however, that the Long Wavelength Array (LWA) and EDGES antennas are expected to have better beams than the one considered here (Bernardi et al., 2015; Mozdzen et al., 2016). We speculate that repeating our analysis using the LWA or the EDGES dipole beams may lead to a spectrum whose frequency structure is less dominated by the beam features and could, therefore, be more sensitivie to a intrinsic difference in the foreground model.

Bibliography

Barkana R., 2018, Nature, 555, 71

Bennett C. L., Halpern M., Hinshaw G., Jarosik N., Kogut A., Limon M., Meyer et al., 2003, The Astrophysical Journal Supplement Series, 148

Bernardi G., McQuinn M., Greenhill L., 2015, The Astrophysical Journal, 799, 90

Bernardi G., Zwart J., Price D., Greenhill L., Mesinger A., Dowell J., Eftekhari T., Ellingson et al., 2016, Monthly Notices of the Royal Astronomical Society, 461, 2847

Beuermann K., Kanbach G., Berkhuijsen E., 1985, Astronomy and Astrophysics, 153, 17

Bowman J. D., Morales M. F., Hewitt J. N., 2009, The Astrophysical Journal, 695, 183

Bowman J. D., Rogers A. E., 2010, Nature, 468, 796

Bowman J. D., Rogers A. E., Monsalve R. A., Mozdzen T. J., Mahesh N., 2018, Nature, 555, 67

Bridle A., Baldwin J., 1967, Monthly Notices of the Royal Astronomical Society, 136, 219

Burns J. O., Bradley R., Tauscher K., Furlanetto S., Mirocha J., Monsalve R., Rapetti D., Purcell et al., 2017, The Astrophysical Journal, 844, 33

Callingham J., Ekers R., Gaensler B., Line J., Hurley-Walker N., Sadler E., Tingay S., Hancock et al., 2017, The Astrophysical Journal, 836, 174

Caswell J., Lerche I., 1979, Monthly Notices of the Royal Astronomical Society, 187, 201

Ciardi B., Ferrara A., White S., 2003, Monthly Notices of the Royal Astronomical Society, 344

Cohen J. G., Hogg D. W., Blandford R., Cowie L. L., Hu E., Songaila A., Shopbell P., Richberg K., 2000, The Astrophysical Journal, 538, 29

De Breuck C., Van Breugel W., Röttgering H. J., Miley G., 2000, Astronomy and Astrophysics Supplement Series, 143, 303

de Oliveira-Costa A., Tegmark M., Gaensler B., Jonas J., Landecker T., Reich P., 2008, Monthly Notices of the Royal Astronomical Society, 388, 247

Dillon J. S., Liu A., Williams C. L., Hewitt J. N., Tegmark M., Morgan E. H., Levine A. M., Morales M. F., Tingay S. J., Bernardi G., et al., 2014, Physical Review D, 89, 023002

Fialkov A., Barkana R., Visbal E., 2014, Nature, 506, 197

Fialkov A., Loeb A., 2013, Journal of Cosmology and Astroparticle Physics, 2013, 066

Field G. B., 1959, The Astrophysical Journal, 129, 536

Furlanetto S. R., 2006, Monthly Notices of the Royal Astronomical Society, 371

Furlanetto S. R., 2016, The 21-cm Line as a Probe of Reionization. Springer

Furlanetto S. R., Oh S. P., Briggs F. H., 2006, Physics Reports, 433

Gleser L., Nusser A., Benson A. J., 2008, Monthly Notices of the Royal Astronomical Society, 391, 383

Górski K. M., Hivon E., Banday A. J., Wandelt B. D., Hansen F. K., Reinecke M., Bartelmann M., 2005, The Astrophysical Journal, 622, 759

Greenhill L., Bernardi G., 2012, arXiv:1201.1700

Güsten R., Mezger P., 1982, Vistas in Astronomy, 26, 159

Harker G., 2012, in American Astronomical Society Meeting Abstracts 220 Vol. 220, Mcmc signal extraction for 21-cm global signal experiments

Haslam C. G. T., Salter C. J., Stoffel H., Wilson W. E., 1982, Astronomy and Astrophysics, 47

He L. P., 2009, Research in Astronomy and Astrophysics, 9, 653

Hills R., Kulkarni G., Meerburg P. D., Puchwein E., 2018, arXiv e-prints

Iliev I. T., Shapiro P. R., Ferrara A., Martel H., 2002, The Astrophysical Journal Letters, 572

Ilovaisky S. A., Lequeux J., 1972, Astronomy and Astrophysics, 18, 169

Jelić V., 2010, arXiv:1008.4356

Jelić V., Zaroubi S., Labropoulos P., Bernardi G., De Bruyn A., Koopmans L. V., 2010, Monthly Notices of the Royal Astronomical Society, 409, 1647

Jelić V., Zaroubi S., Labropoulos P., Thomas R. M., Bernardi G., Brentjens M. A., De Bruyn A., Ciardi et al., 2008, Monthly Notices of the Royal Astronomical Society, 389, 1319

Jelić V., Zaroubi S., Labropoulos P., Thomas R. M., Bernardi G., Brentjens M. A., De Bruyn A., Ciardi B., Harker G., Koopmans L. V., et al., 2008, Monthly Notices of the Royal Astronomical Society, 389, 1319

Kerrigan J., Pober J., Ali Z., Cheng C., Parsons A., Aguirre J., Barry N., Bradley R., Bernardi G., Carilli C., et al., 2018, arXiv preprint arXiv:1801.00460

Liu A., Pritchard J. R., Tegmark M., Loeb A., 2013, Physical Review D, 87

Liu A., Tegmark M., 2011, Physical Review D, 83, 103006

Loeb A., Zaldarriaga M., 2004, Physical Review Letters, 92

McQuinn M., Switzer E. R., 2009, Physical Review D, 80

Madau P., Meiksin A., Rees M. J., 1997, The Astrophysical Journal, 475, 429

Mezger P. G., Pauls T., 1979, HII regions and star formation in the galactic center. Vol. 84

Mirocha J., Harker G. J., Burns J. O., 2015, The Astrophysical Journal, 813, 11

Monsalve R. A., Rogers A. E., Bowman J. D., Mozdzen T. J., 2017, The Astrophysical Journal, 847, 64

Morales M. F., Bowman J. D., Hewitt J. N., 2006, The Astrophysical Journal, 648, 767

Morandi A., Barkana R., 2012, Monthly Notices of the Royal Astronomical Society, 424, 2551

Mozdzen T. J., Bowman J. D., Monsalve R. A., Rogers A. E. E., 2016, Monthly Notices of the Royal Astronomical Society, 455, 3890

Mozdzen T. J., Bowman J. D., Monsalve R. A., Rogers A. E. E., 2017, Monthly Notices of the Royal Astronomical Society, 464, 4995

Nunhokee C., Bernardi G., Kohn S., Aguirre J., Thyagarajan N., Dillon J., Foster G., Grobler et al., 2017, The Astrophysical Journal, 848, 47

Paciga G., Chang T. C., Gupta Y., Nityanada R., Odegova J., Pen U. L., Peterson J. B., Roy J., et al., 2011, Monthly Notices of the Royal Astronomical Society, 413, 1174

Parsons A. R., Backer D. C., Foster G. S., Wright M. C., Bradley R. F., Gugliucci N. E., Parashare C. R., Benoit E. E., Aguirre J. E., Jacobs D. C., et al., 2010, The Astronomical Journal, 139, 1468

Parsons A. R., Backer D. C., Foster G. S., Wright M. C. H., Bradley R. F., Gugliucci N. E., Parashare C. R., Benoit E. E., et al., 2010, The Astronomical Journal, 139, 1468

Patra N., Subrahmanyan R., Sethi S., Shankar N. U., Raghunathan A., 2015, The Astrophysical Journal, 801, 138

Pober J., Hazelton B., Beardsley A., Barry N., Martinot Z., Sullivan I., Morales M., Bell et al., 2016, The Astrophysical Journal, 819, 8

Price D., Greenhill L., Fialkov A., Bernardi G., Garsden H., Barsdell B., Kocz J., Anderson et al., 2018, Monthly Notices of the Royal Astronomical Society, 478, 4193

Pritchard J. R., Furlanetto S. R., 2007, Monthly Notices of the Royal Astronomical Society, 376, 1680

Pritchard J. R., Loeb A., 2010, Physical Review D, 82

Pritchard J. R., Loeb A., 2012, Reports on Progress in Physics, 75

Remazeilles M., Dickinson C., Banday A., Bigot-Sazy M.-A., Ghosh T., 2015, Monthly Notices of the Royal Astronomical Society, 451, 4311

Roger R., Costain C., Landecker T., Swerdlyk C., 1999, Astronomy and Astrophysics Supplement Series, 137, 7

Rogers A. E., Bowman J. D., 2008, The Astronomical Journal, 136, 641

Rottgering H. J., Braun R., Barthel P., Van Haarlem M., Miley G., Morganti R., Snellen I., Falcke et al., 2006, arXiv

Sadler E. M., Jackson C. A., Cannon R. D., McIntyre V. J., Murphy T., Bland-Hawthorn J., Bridges T., Cole et al., 2002, Monthly Notices of the Royal Astronomical Society, 329, 227

Santos M. G., Cooray A., Knox L., 2005, The Astrophysical Journal, 625, 575

Scott D., Rees M., 1990, Monthly Notices of the Royal Astronomical Society, 247, 510

Shaver P. A., Windhorst R. A., Madau P., de Bruyn A. G., 1999, Astronomy and Astrophysics, 345, 380

Singh S., Subrahmanyan R., Shankar N. U., Rao M. S., Fialkov A., Cohen A., Barkana R., Girish et al., 2017, The Astrophysical Journal Letters, 845

Sokolowski M., Tremblay S. E., Wayth R. B., Tingay S. J., Clarke N., Roberts P., Waterson M., Ekers et al., 2015, Publications of the Astronomical Society of Australia, 32

Tingay S., Goeke R., Bowman J. D., Emrich D., Ord S., Mitchell D. A., Morales M. F., Booler et al., 2013, Publications of the Astronomical Society of Australia, 30

Tozzi P., Madau P., Meiksin A., Rees M. J., 2000, The Astrophysical Journal, 528, 597

Trott C. M., Pindor B., Procopio P., Wayth R. B., Mitchell D. A., McKinley B., Tingay S. J., Barry et al., 2016, The Astrophysical Journal, 818, 139

Vedantham H., Shankar N. U., Subrahmanyan R., 2012, The Astrophysical Journal, 745, 176

Voytek T. C., Natarajan A., García J. M. J., Peterson J. B., López-Cruz O., 2014, The Astrophysical Journal Letters, 782

Wang J., Xu H., An T., Gu J., Guo X., Li W., Wang Y., Liu C., Martineau-Huynh O., Wu X.-P., 2013, The Astrophysical Journal, 763, 90

Wang X., Tegmark M., Santos M. G., Knox L., 2006, The Astrophysical Journal, 650, 529

Wouthuysen S., 1952, The Astronomical Journal, 57, 31

Zaroubi S., 2012, arXiv:1206.0267